STATISTICAL MODES AND PHYSICAL DRIVERS OF MULTIDECADAL SEA SURFACE TEMPERATURE VARIABILITY IN THE NORTHWEST ATLANTIC

by

Jonathan Coyne

Submitted in partial fulfillment of the requirements
for the degree of Master of Science

at

Dalhousie University
Halifax, Nova Scotia
February 2022

TABLE OF CONTENTS

LIST OF TABLES

LIST OF FIGURES

ABSTRACT

Variations in ocean temperature and the presence of large multidecadal sea surface temperature (SST) oscillation can have a severe impact on Northwest Atlantic ecosystems and fisheries. Differences between historical SST datasets in the regions have also been consistently noted. It is imperative that steps be taken to consider cross-dataset variability when determining patterns of variability in Northwest Atlantic SST. First, from 1901 to 2010 a novel combined-dataset approach was used along with an extended empirical orthogonal function (EEOF) analysis to determine the role of anthropogenic forcing of SST along with leading modes of variability over the Northwest Atlantic shelf and slope. Second, a mixed-layer heat budget from 1850 to 2015 was used to determine the dominant physical processes driving yearly-to-multidecadal variability across the Northwest Atlantic shelf and slope. Results from the EEOF suggest that positive Atlantic Multidecadal Oscillation (AMO) years are driven by positive North Atlantic Oscillation years (NAO).

LIST OF ABBREVIATIONS AND SYMBOLS USED

Abbreviation	Full Name
RCP	Representative Concentration Pathway
SST	Sea Surface Temperature
SSTA	Sea Surface Temperature Anomaly
AMO	Atlantic Multidecadal Oscillation
NAO	North Atlantic Oscillation
ICOADS	International Comprehensive Atmosphere-Ocean Data Set
EOF	Empirical Orthogonal Function
PC	Principal Component
EEOF	Extended Empirical Orthogonal Function
ToE	Time of Emergence
HadISST V1.1	Hadley Centre Sea Ice and Sea Surface Temperature data set version 1.1
ERSST V5	Extended Reconstructed Sea Surface Temperature version 5
COBE	Centennial In Situ Observation Based Estimates
CERA-20C	Coupled Reanalysis of the Twentieth Century
SODA	Simple Ocean Data Assimilation system
CESM-LENS	Community Earth System Model - Large Ensemble
CESM2-LENS	Community Earth System Model version 2 - Large Ensemble
CPC	Cumulative Principal Component

ACKNOWLEDGEMENTS

Thank you to Eric Oliver and the research committee for the guidance they gave me throughout the completion of my Masters degree. Thank you to my Mom, my brothers, my good friend Rory, and my girlfriend Amy, for their constant support over the last two years.

CHAPTER 1

GENERAL INTRODUCTION

1.1 Motivation

Anthropogenically-induced climate change is leading to increased ocean temperatures throughout most of the world (*Loder and Wang*, 2015, 2019; *Bindoff et al.*, 2019; *Alexander et al.*, 2020). Earth system models predict that sustaining our current level of greenhouse gas emissions under the Representative Concentration Pathway (RCP) 8.5, will lead to a significant change in the ocean state over the coming century (*Henson et al.*, 2017; *Bindoff et al.*, 2019). Under this pathway, significant impacts to ocean life and coastal communities are also predicted (*Bindoff et al.*, 2019). Given the expected increase in ocean temperature over the coming century (*Loder and Wang*, 2015, 2019; *Bindoff et al.*, 2019; *Alexander et al.*, 2020), it has become necessary to understand and be able to predict yearly-to-multidecadal sea surface temperature (SST) variability in the Northwest Atlantic in the context of increasing global ocean temperature.

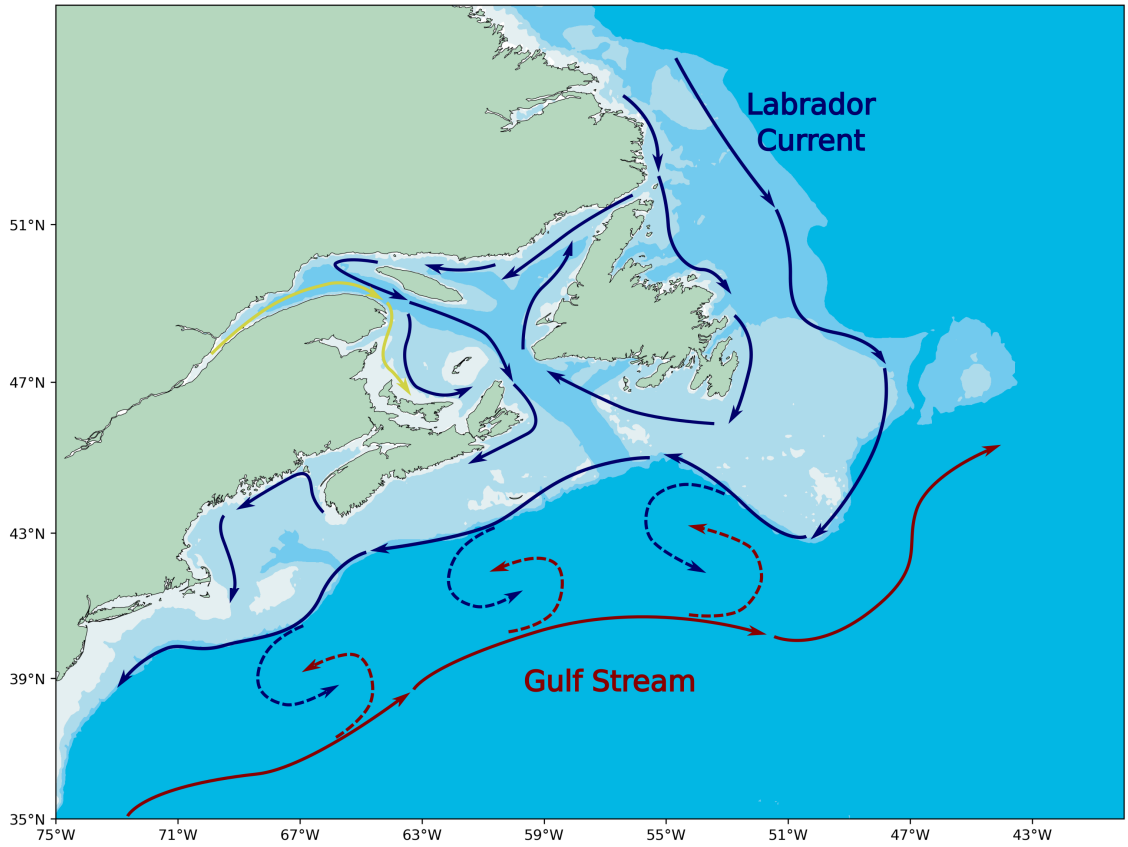

Figure 1.1: General circulation and bathymetry of the Northwest Atlantic. The solid blue and red arrows show the general path of the Labrador Current and Gulf Stream respectively. The dashed blue and red arrows mark areas of mixing between the Labrador Current and the Gulf Stream. The yellow arrows show the general path of the St. Lawrence River outflow.

1.2 Northwest Atlantic Trends and Variabilility

Multidecadal oscillations are a well known feature of Northwest Atlantic SST, in part due to the general circulation of the region (*Petrie and Drinkwater*, 1993; *Loder and Petrie*, 1998; *Deser et al.*, 2010; *Loder and Wang*, 2015, 2019). The Gulf Stream brings warm, relatively salty water from the south (*Loder and Petrie*, 1998; *Chen et al.*, 2014, 2020) (Fig. 1.1, red arrows). It runs along the shelf towards Cape Hatteras before heading eastward towards Europe. Often warm-core rings form in the slope regions between the continental shelf and Gulf Stream before travelling westward (*Chen et al.*, 2014, 2020). The movement of warm-core rings into the shelf regions of the Northwest Atlantic between

the Mid-Atlantic Bight and the Grand Banks, can have a significant influence on shelf SST (*Chen et al.*, 2014). To the north, the Labrador Current brings cool fresh water from the Arctic along the Northwest Atlantic Shelf down to and sometimes further south than the Scotian Shelf (*Han*, 2003; *Loder and Petrie*, 1998; *Han et al.*, 2014; *Chen et al.*, 2020) (Fig. 1.1, blue arrows). The relative strength of both the Gulf Stream and Labrador Current changes over time resulting in significant changes to SST and SST anomaly (SSTA) (*Deser et al.*, 2010; *Han et al.*, 2014; *Loder and Wang*, 2015, 2019). Converging ocean currents along with other oceanic/atmospheric factors, result in the Northwest Atlantic shelf and slope showing the highest interannual-to-multidecadal variability in the North Atlantic (*Petrie and Drinkwater*, 1993; *Deser et al.*, 2010; *Han et al.*, 2014). The relative strength of the Labrador Current and Gulf Stream are represented in climate mode indices relevant in the Northwest Atlantic shelf and slope.

Climate modes have been used to define potentially-predictable patterns of oceanic and atmospheric variability (*Deser et al.*, 2010; *Loder and Wang*, 2015, 2019). A climate mode consists of some oceanic/atmospheric variable spatial pattern with which a time series is associated (*Hurrell et al.*, 2003; *Trenberth and Shea*, 2006). Northwest Atlantic SSTA is dominated by two climate modes; the Atlantic Multidecadal Oscillation (AMO) and North Atlantic Oscillation (NAO) (*Deser et al.*, 2010; *Loder and Wang*, 2015, 2019).

The AMO is a large-scale climate mode exhibiting multidecadal variability on an associated SST polar-structured spatial pattern covering most of the North Atlantic on timescales of 60-70 years (*Deser et al.*, 2010; *Loder and Wang*, 2015, 2019). The AMO is considered to be a natural mode of oscillation in Atlantic thermohaline circulation with potential influences from surface air temperatures and anthropogenically-induced climate change. The AMO has been related to decreases in SST in the Northwest Atlantic from 1950 to 1970, followed by increases in SST from 1980 to 2000. The AMO has also been known to "stall" or increase the rate of anthropogenically-induced SST warming in the Northwest Atlantic depending on its phase (*Loder and Wang*, 2015). It should be noted

that the physical forcings behind the AMO are still debated (*Deser et al.*, 2010; *Loder and Wang*, 2015). This is partially due to the long timescale on which the AMO oscillates and the corresponding lack of available data over this period. Given that many of the oceanic/atmospheric variables needed to determine the forcing behind AMO changes are not observed over many AMO cycles (if any), this makes the analysis of potential forcing difficult.

The NAO refers to yearly-to-decadal changes in sea level pressure between the Arctic and the Atlantic subtropics forced by the redistribution of atmospheric mass (*Marshall et al.*, 2001; *Visbeck et al.*, 2003; *Deser et al.*, 2010). The effect of the NAO on North Atlantic SSTA is characterized as a tripolar structure, with negative anomalies in the subpolar North Atlantic and subtropics, and positive anomalies in the mid-latitudes (*Deser et al.*, 2010). During negative index years, both the Iceland low pressure cell and Azores high pressure cell are weakened (*Marshall et al.*, 2001; *Visbeck et al.*, 2003). This change in sea level pressure is accompanied by changes in wind, air temperature, and precipitation (*Deser et al.*, 2010). Increased transport of Labrador shelf water westward along the Northwest Atlantic shelf regions has been attributed to consistent negative NAO index years (*Petrie*, 2007).

Over the last half century, anomalously high warming has also been noted in Northwest Atlantic shelf and slope SST, especially in the Scotian Shelf and Grand Banks (*Shearman and Lentz*, 2010; *Loder and Wang*, 2015). Warming trends in Northwest Atlantic SST and mixed layer temperature have been noted in datasets going back before 1900 with trends increasing in recent years (*Loder and Wang*, 2015, 2019). While the recent increase is worrying, it is important to note that multidecadal oscillation in SST has the ability to significantly influence short-term SST trends (*Loder and Wang*, 2019; *Bindoff et al.*, 2019). It is therefore important to consider natural SST variability when determining long-term trends or when studying the role of anthropogenically-induced climate change in Northwest Atlantic SST (*Overland and Preisendorfer*, 1982; *Henson et al.*, 2017).

The combination of warming trends and large multidecadal oscillation makes the area especially susceptible to extreme SST events (*Petrie and Drinkwater*, 1993; *Loder and Wang*, 2015, 2019; *Holbrook et al.*, 2019), while also underlining the importance of understanding and being able to predict Northwest Atlantic SST trends and variability. Given the historic and current environmental and economic importance of the area, extreme SST events have the potential to have a large-scale impact on local populations and ecosystems (*Mills et al.*, 2013; *Oliver et al.*, 2021). *Coumou and Rahmstorf* (2012) suggest that anthropogenic climate change, in combination with multidecadal oscillation, will cause an increase in the severity and frequency of extreme SST events globally, including the Northwest Atlantic. Past extreme SST events in the Northwest Atlantic have caused significant impacts on local marine ecosystems and marine-focused sections of the economy. In 2012, a "severe" marine heatwave occurred in the Northwest Atlantic (*Hobday et al.*, 2018). Changes in the phenology, distribution, and population of American Lobsters as a result of the marine heatwave led to a decrease in market value, as well as tensions between Canadian and United States fishing industries (*Mills et al.*, 2013).

1.3 Availability of Observations and Model Output

Compared to most other areas of the world, the Northwest Atlantic shelf and slope have a relatively high number of SST observations going back over 150 years (*Deser et al.*, 2010; *Kent et al.*, 2021). These SST observations, often recorded from lighthouses or passing ships, are collected in large quality-controlled datasets, such as the International Comprehensive Atmosphere-Ocean Datas Set (ICOADS) (*Deser et al.*, 2010; *Kent et al.*, 2021). The observation-based datasets can then be used to create spatially complete global gridded data products such as HadISST V1.1 and SODA (*Rayner et al.*, 2003; *Giese et al.*, 2016). Global gridded data products often use statistical interpolation or physically-derived numerical models to fill in grid cells to create a spatially complete SST record (*Rayner et al.*, 2003; *Hirahara et al.*, 2014; *Giese et al.*, 2016; *Huang et al.*, 2017; *Laloyaux et al.*,

2018). Missing measurements mean that data products lack dynamical consistency as the interpolation/modelling methods do not perfectly predict ocean/atmospheric variables (*Kent et al.*, 2021). This makes the use of global gridded data products to analyze physical processes, such as heat budgets, difficult, as errors in temperature tendency are cumulatively summed over the entire heat budget time period (*Stevenson and Niiler*, 1983). After 1980, the use of satellite-based SST measurements allowed for the creation of spatially complete SST records (*Rayner et al.*, 2003; *Deser et al.*, 2010). Differences between global gridded data products have been noted in the past resulting from data sparcity, interpolation methods, and corrections to the source data (*Deser et al.*, 2010; *Loder and Wang*, 2015, 2019). Historically, modes of variability in the Northwest Atlantic have been defined from a single data product and do not consider cross-dataset variability or consistency (*Loder and Wang*, 2015, 2019).

Another common tool for studying SST variability is ocean and climate model output (*Petrie and Drinkwater*, 1993; *Han*, 2003; *Wills et al.*, 2019; *Alexander et al.*, 2020). Ocean and climate models use theory solved numerically by a computer, sometimes using observations as initial and boundary conditions (*Wills et al.*, 2019; *Rodgers et al.*, 2021). The complexity of the model can vary, with some earth system models including coupled land, ocean, atmosphere, and sea ice models (*Wills et al.*, 2019; *Rodgers et al.*, 2021). The use of earth system model output allows for a dynamically consistent record of multiple ocean/atmospheric variables including SST with no missing data. Unfortunately, models never recreate observed SST variability perfectly (*Roemmich et al.*, 2005). For this reason, special consideration must be taken to ensure that the earth system model output accurately reflects observations.

1.4 Thesis Overview

In this thesis, long-term trends and modes of SST variability along the Northwest Atlantic shelf and slope were determined with the aim of better understanding the amplitude and

phasing of yearly-to-multidecadal variability and its physical drivers and relationship to regional circulation and the role of the AMO and NAO. Chapter 2 uses a novel, multi-dataset approach to determine long-term trends and yearly-to-multidecadal variability in Northwest Atlantic shelf and slope SSTA. The aim is to determine modes of SSTA variability and the emergence of the anthropogenically-caused climate change signal while using cross-dataset variability to better constrain uncertainties on both. Following this, Chapter 3 uses the Community Earth System Model 2 - Large Ensemble (CESM2-LENS) output to create a mixed layer temperature heat budget of the Northwest Atlantic shelf and slope regions from 1850 to 2015. The aim is to better understand the physical forcing behind yearly-to-multidecadal variability, including the AMO and NAO climate modes, over multiple cycles. Lastly, in Chapter 4 I discuss the findings of the previous two chapters and present overall conclusions.

CHAPTER 2

TRENDS AND MULTIDECADAL VARIABILITY IN NORTHWEST ATLANTIC SEA SURFACE TEMPERATURE FROM MULTIPLE DATA SETS

2.1 Introduction

Both warming trends and a large multidecadal oscillation have been identified in historical Northwest Atlantic SST records (*Petrie and Drinkwater*, 1993; *Loder and Wang*, 2015, 2019). This makes the area especially susceptible to extreme SST events (*Holbrook et al.*, 2019), while also underlining the importance of understanding Northwest Atlantic SST trends and variability. Given the historic and current environmental and economic importance of the area, extreme SST events have the potential to have a large-scale impact on local populations and ecosystems (*Mills et al.*, 2013).

SST warming from 1870 to 2011 can be seen throughout the Northwest Atlantic, excluding the area around Greenland, where negative trends are observed (*Loder and Wang*, 2015). However, caution must be taken, as the long-term linear trend of SST in the Northwest Atlantic is dependent on the time period over which it is calculated, due to the presence of a large multidecadal oscillation (*Loder and Wang*, 2015). *Coumou*

and Rahmstorf (2012) suggest that anthropogenic climate change, in combination with multidecadal oscillation, will cause an increase in the severity and frequency of extreme SST events in the Northwest Atlantic.

The AMO is a large-scale climate mode exhibiting multidecadal variability in SST on timescales of 60-70 years (*Deser et al.*, 2010; *Loder and Wang*, 2015). The AMO is considered to be a natural mode of oscillation in Atlantic Meridional Overturning Circulation with potential influences from surface air temperatures and anthropogenically-induced climate change. The AMO has been related to decreases in SST in the Northwest Atlantic from 1950 to 1970, followed by increases in SST from 1980 to 2000. The AMO has also been known to "stall" or increase the rate of anthropogenically-induced SST warming in the Northwest Atlantic depending on its phase (*Loder and Wang*, 2015). Positive AMO years may occur as the result of consistent negative air-sea heat flux over the Labrador Sea driving the Atlantic Meridional Overturning Circulation to advect warm water north (*Wills et al.*, 2019). This leads to anomalously warm ocean temperatures throughout the Atlantic and the formation of a low pressure cell. With time, the Atlantic Meridional Overturning Circulation over-corrects the initial cold water scenario leading to increased stratification in the Labrador Sea. This weakens the Atlantic Meridional Overturning Circulation and causes the dissipation of the positive AMO event. It should be noted that the physical forcings behind the AMO are still debated (*Deser et al.*, 2010; *Loder and Wang*, 2015).

The NAO refers to yearly-to-decadal changes in sea level pressure between the Arctic and the Atlantic subtropics forced by the redistribution of atmospheric mass (*Visbeck et al.*, 2003; *Marshall et al.*, 2001; *Deser et al.*, 2010). The effect of the NAO on North Atlantic SSTA is characterized as a tripolar structure, with negative anomalies in the subpolar North Atlantic and subtropics, and positive anomalies in the middle latitudes (*Deser et al.*, 2010). The combined latent and sensible heat flux mirrors this tripolar structure and so the ocean loses heat energy to the atmosphere in the subpolar North Atlantic. This is the

result of the changes in sea level pressure, which during positive index years results in a strengthened Iceland low pressure cell and Azores high pressure cell. The strengthening of the pressure cells results in anomalously strong midlatitude westerlies and northeast trade winds. Meanwhile, at middle latitudes the ocean gains heat energy from the atmosphere as a result of weakened wind speeds. Anomalous wind speeds and the resulting Ekman transport can also strengthen the Gulf Stream and Labrador Current during positive years (*Deser et al.*, 2010). During negative index years, both the Iceland low pressure cell and Azores high pressure cell are weakened (*Visbeck et al.*, 2003; *Marshall et al.*, 2001). This change in sea level pressure is accompanied by changes in wind, air temperature, and precipitation (*Deser et al.*, 2010). Increased transport of Labrador shelf water westward along the Northwest Atlantic shelf regions has been attributed to consistent negative NAO index years (*Petrie*, 2007).

Past studies have used empirical orthogonal functions (EOFs) to determine modes of variability in SST in the Northwest Atlantic (*Deser et al.*, 2010; *Loder and Wang*, 2015, 2019). Results from EOFs in the region have differed across SST datasets as a result of data sparsity, interpolation methods, and corrections to the source data. Interpretation of EOF results is often done by correlating the resulting principal components (PCs) time series with known climate modes (e.g., AMO, NAO) (*Loder and Wang*, 2015, 2019). This makes it difficult to relate EOF results to specific oceanic and atmospheric variables in the region as statistics does not necessarily correspond to the physics. *Loder and Wang* (2015, 2019) found significant correlation between the leading two modes of a North Atlantic SSTA EOF analysis with AMO and NAO (corresponding to the first and second mode respectively).

This chapter will use a novel, multi-dataset approach to determine the role of long-term trends and yearly to multidecadal variability in Northwest Atlantic shelf and slope SST. The use of multiple datasets will allow for the consideration of cross-dataset variability that has been noted in in previous EOF results (*Loder and Wang*, 2015, 2019). SST

has been gathered from 5 different observation-based datasets and one global climate model. Regions of interest on the slope and shelf will be defined from Cape Hatteras, North Carolina, to Cape Chidley, Labrador. Spatially averaged SST in these regions of interest will be decomposed into a climatology, linear trend, and SSTA. Time series of SSTA including linear trends will be created to determine the role of anthropogenically-induced climate change along the slope and shelf regions of the Northwest Atlantic. Long-term increases in SSTA have been identified in all regions of interest under the RCP 8.5 emissions scenario. The time of emergence of the anthropogenic warming from the natural variability for each region of interest was also determined. An extended empirical orthogonal function (EEOF) will then be performed on the spatially averaged SSTA (excluding linear trend) in the regions of interest to determine the modes of SSTA variability in the slope and shelf regions of the Northwest Atlantic. Spatial and temporal areas with high cross-dataset uncertainty in EEOF results will also be identified. Finally, correlation coefficients will be determined between PC time series and oceanic and atmospheric variables in order to explore the relationship between the two. Evidence is found to support the findings of previous studies' on the physical forcing behind the SSTA spatial pattern associated with the AMO and NAO, and that the forcing may extend to the shelf and slope regions of the Northwest Atlantic.

2.2 Data

2.2.1 Observation-Based Data Products

Monthly SST was obtained from five observation-based datasets (Table 2.1). HadISST V1.1 (*Rayner et al.*, 2003), ERSST V5 (*Huang et al.*, 2017), and COBE SST (*Hirahara et al.*, 2014) use historical SST measurements and statistical interpolation methods to create spatially and temporally complete observation-based datasets. CERA-20C (*Laloyaux et al.*, 2018) and SODA (*Giese et al.*, 2016) are both ocean re-analysis datasets which combine numerical ocean models with historical SST recordings, via data assimilation, to create a

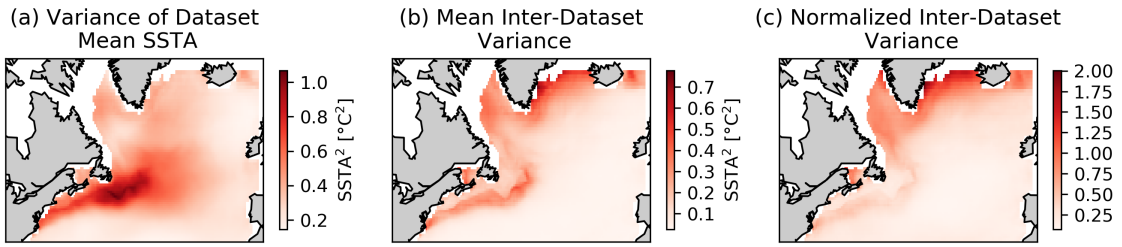

Figure 2.1: SST variability in the Northwest Atlantic. (a) The variance over time of the dataset mean SSTA timeseries at each pixel, (b) the variance across dataset estimates, averaged over time, at each pixel, (c) the ratio of b over a.

spatially and temporally complete observation-based datasets.

Each dataset was interpolated to a common spatial grid (0.5° longitude by 0.5° latitude) in order to create the combined dataset. The variance of the inter-dataset mean SSTA was taken over the entire shared time period in order to measure SSTA variability over the Northwest Atlantic (Fig. 2.1a). Variability is highest along the shelf regions of the Northwest Atlantic, especially in the Grand Banks. The mean of the inter-dataset SSTA variance is a measure of disagreement across SST products (Fig. 2.1b). Disagreement is highest along the slope regions from the Mid-Atlantic Bight to the Flemish Cap and in the Denmark Strait. The mean inter-dataset variance was then divided by the variance of the inter-dataset mean SSTA to find the normalized inter-dataset variance (Fig. 2.1c). SST dataset disagreement was large in regions of high SST variability and at high latitudes, possibly related to data scarcity. Areas of high disagreement include the Gulf of St. Lawrence, Labrador Sea, Denmark Strait, and Norwegian Sea.

Differences have been noted in past literature when comparing in-situ SST measurements with satellite-derived SST (*O'Carroll et al.*, 2008) as is done here. For the purposes of this paper, no additional corrections will be done to make these diverse datasets more consistent. Results must be interpreted with the above-mentioned differences in mind.

2.2.2 Climate Model Output

SST output was also taken from a non-observation based product, CESM-LENS (Table 2.1), a global climate model (*Kay et al.*, 2015). CESM-LENS provides daily global SST with 40 ensemble members. The CESM-LENS historical run (1920 to 2005) is forced by anthropogenic greenhouse gas emissions and natural forcings. The CESM-LENS future projection run (2005 to 2100) is forced by the RCP8.5 "business as usual" anthropogenic greenhouse gas emissions scenario and projected natural forcings. The CESM-LENS natural control run is only subjected to natural forcings and was allowed to run for 1800 years to provide an estimate of pre-industrial climate variability without anthropogenic influences. The historical and future runs were concatenated together to create one temporally continuous dataset (1920-2100).

In general, the magnitude of SST variability from global climate models is underestimated when compared to instrumental recordings, especially on decadal to multidecadal timescales (*Sachs*, 2007). To address this, the variance of the model SSTA was bias-corrected . SSTA from the observation-based datasets and CESM-LENS historical and future runs were put through a high-pass filter with a 60 year cutoff frequency in order to isolate for multidecadal and higher frequency variability. The ratio of the standard deviations was then found between the observation-based datasets and CESM-LENS historical and future runs over a shared time period. This process was repeated between each dataset and each ensemble. The high-pass filtered CESM-LENS historical and future run data was then multiplied by the ratio (ratio of 1.168 ± 0.378 for all regions of interest), as a bias-correction, and added back to the low frequency variability, which was filtered out initially. The same was done for the CESM-LENS natural control run (ratio of 1.336 ± 0.376 for all regions of interest).

2.2.3 Ocean-Atmosphere State Variables and Climate Modes

Monthly net shortwave radiation (Q_{SW}), net longwave radiation (Q_{LW}), surface sensible heat flux (Q_S), surface latent heat flux (Q_L), evaporation (E), total precipitation (P),

Global Gridded SST Data Products			
Name	Time Range (Monthly)	Grid (Latitude by Longitude)	Number of Ensemble Members
HadISST V1.1	January 1870 to January 2017	1° x 1°	N/A
ERSST V5	January 1854 to December 2017	2° x 2°	N/A
COBE SST	January 1900 to July 2019	1° x 1°	N/A
CERA-20C	January 1901 to December 2010	1° x 1°	10
SODA	January 1900 to December 2013	0.5° x 0.5°	N/A
Global Climate Model			
Section	Time Range (Monthly)	Spatial Resolution (Latitude by Longitude)	Number of Ensemble Members
Historical Run	January 1920 to December 2005	1° x 1°	40
Future Projection Run	January 2006 to December 2100	1° x 1°	40
Natural Control Run	1800 years	1° x 1°	40

Table 2.1: Global monthly gridded SST products and CESM-LENS meta data. Data products/sets which lack multiple ensemble members are labelled as N/A.

surface and depth-averaged salinity (S), surface and depth-averaged ocean velocity ($\vec{u}$), and 10m wind velocity ($\vec{u}_{10}$) was obtained from the SODA and CERA-20C ocean re-analysis data products. The net air-sea heat flux (Q_{Net}) and net freshwater flux (FW_{Net}), not including river runoff, were also determined.

$$Q_{Net} = Q_{SW} + Q_{LW} + Q_S + Q_L \tag{2.1}$$

$$FW_{Net} = E + P \tag{2.2}$$

All heat flux variables are defined as positive downwards. The time range and resolution is consistent with the SST from CERA-20C (Table 2.1).

Ocean/atmosphere state variables were selected based on the terms in the surface mixed-layer heat budget. A heat budget equation can be used to determine the processes behind variations in SST (*Stevenson and Niiler*, 1983). Using the conservation of heat and mass equations, a final mixed-layer heat budget equation can be derived which shows that variations in SST are equal to the sum of horizontal and vertical advection, air-sea heat flux, and horizontal and vertical diffusion (see Appendix B). Advection and air-sea heat flux terms are commonly the most important in regards to variations in SST. Therefore, terms relevant to the advection ($\vec{u}$, $\vec{u}_{10}$) and air-sea heat flux (Q_{SW},Q_{LW},Q_S,Q_L) will be compared to results from the EEOF.

The monthly AMO index (1870 to 2010) and NAO index (1865 to 2019) was collected from *Trenberth and Shea* (2006) and *Hurrell et al.* (2003) respectively. Both the AMO and NAO were averaged to yearly.

2.3 Methods

2.3.1 Regions of Interest

In order to determine the meridional and temporal structure of SSTA in the Northwest Atlantic shelf and slope region, specific regions of interest were defined using local

bathymetry following *Richaud et al.* (2016) and *Chen et al.* (2020) (Fig. 2.2). The regions extend meridionally from Cape Hatteras, North Carolina, to Cape Chidley, Labrador. Regions 1-14 correspond to the Northwest Atlantic shelf (0 - 1000m depth). Regions 1-3 are associated with the Mid-Atlantic Bight, 4-5 with the Gulf of Maine, 6-7 with the Scotian Shelf, 8-9 with the Gulf of St. Lawrence, 10-11 with the Grand Banks and Flemish Cap, and 12-14 with the Northern Newfoundland Coast and Labrador Shelf.

Regions 15-21 correspond to the Northwest Atlantic slope (4000m+ depth) and are restricted to be south of 45°N as slope waters along the Labrador Shelf are difficult to define (*Chen et al.*, 2020). The slope regions also follow the general path of the Gulf Stream. Given the coarse resolution of some observation-based datasets (Table 2.1), the size of the slope regions of interest had to be modified so at least one gridcell of each dataset was included in each region of interest. SST and oceanic/atmospheric variables were spatially averaged over each of the defined regions of interest.

2.3.2 Statistical Decomposition of Sea Surface Temperature

SST was considered to be a sum of three components:

$$T(t) = T^{\mathrm{Tr}}(t) + T^{\mathrm{s}}(t) + T'(t) \tag{2.3}$$

where $T(t)$ is the SST at time t, $T^{\mathrm{Tr}}(t)$ is the linear SST trend at time t, $T^{\mathrm{s}}(t)$ is the SST seasonal cycle (climatology) at time t, and $T^{'}(t)$ is the SSTA at time t. The linear SST trend, $T^{\mathrm{Tr}}(t)$, was calculated by least square regression over the entire SST time period. The climatology, $T^{\mathrm{s}}(t)$, calculated by finding the mean SST for each month from 1920 to 1950 (*Loder and Wang*, 2015; *Lotze et al.*, In Review), was then subtracted from the SST for all datasets excluding the CESM-LENS natural control run (Table 2.1), to find the SSTA with long term trend, $T^{\mathrm{Tr}}(t) + T'(t)$. For the CESM-LENS and datasets with multiple ensemble members, the ensemble mean and standard deviation was calculated after the climatology was removed. Given that this thesis is partially part of the COD-REMAP

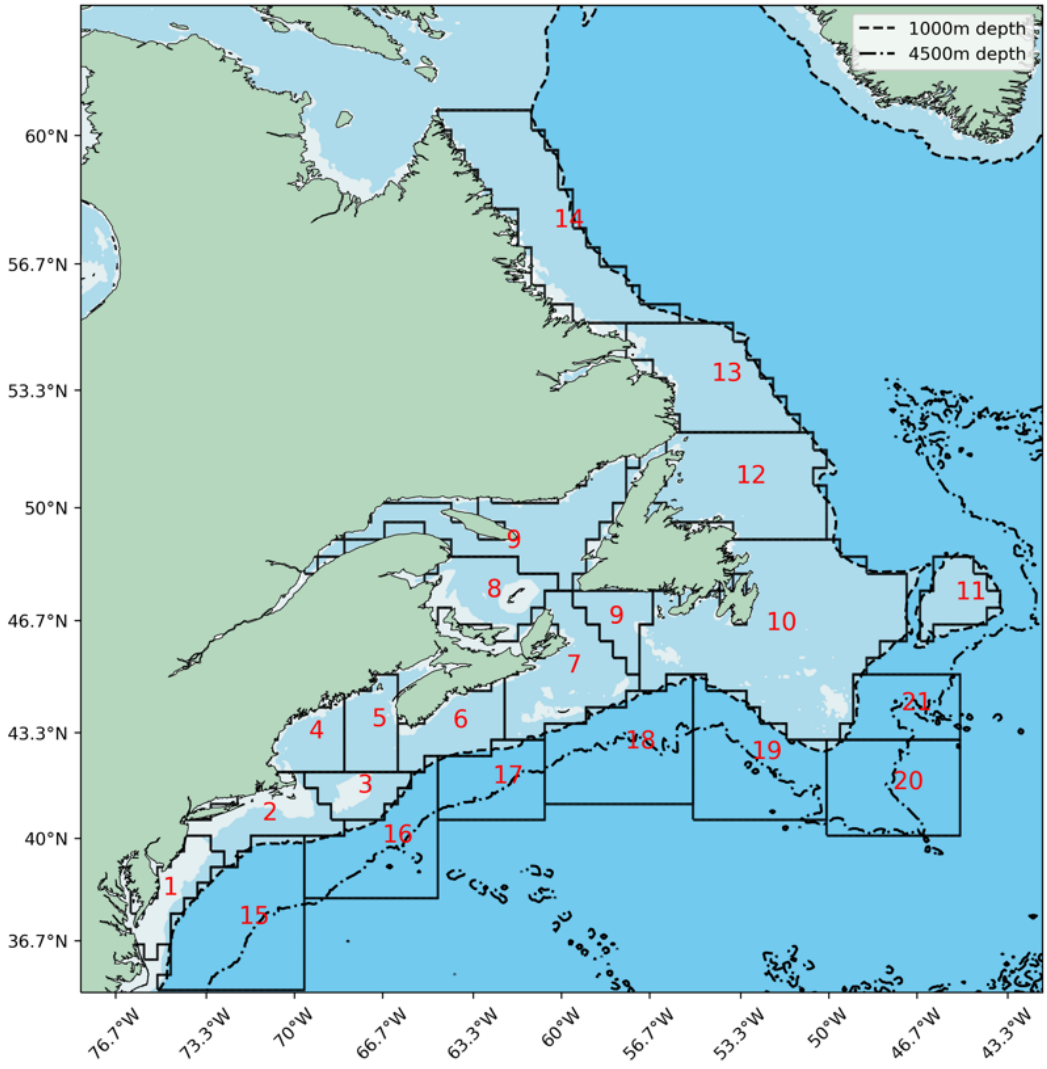

Figure 2.2: Northwest Atlantic shelf and slope regions of interest on top of local bathymetry. Regions are outlined by solid black lines, 1000 meters depth is given by the dashed line, 4500 meters depth is given by the dash dot line. Specific regions are numbered from 1 to 21 in red with 1 to 14 being shelf regions and 15 to 21 being slope regions. The area south of Western Newfoundland, is part of region 9.

project, the period over which the climatology was calculated matches that used in *Lotze et al.* (In Review). A climatology for the CESM-LENS natural control run was calculated for the entire 1800 year time period and then subtracted from the original SST. After the climatology had been calculated and removed, monthly SSTA was temporally averaged to yearly SSTA. The same decomposition was performed on the oceanic/atmospheric variables. *Lotze et al.* (In Review)

The range of natural climate variability (without the temperature influence of humans on the climate system) was determined from the standard deviation of the CESM-LENS natural control run. 68% of the natural variability is contained within ± 1 standard deviation assuming a normal distribution.

2.3.3 Time of Emergence

In order to determine when the CESM-LENS historical and future runs SSTA surpasses natural variability in a specific region for the remainder of a particular time series, a time of emergence is calculated. Using the definition brought forward by *Henson et al.* (2017), the time of emergence is the year where the SSTA exceeds 95% of the natural variability consistently for the rest of the time series. First, a date in the time series where the climate change signal begins is determined by finding where the cumulative sum of the SSTA gradient exceeds 0 for the remainder of the time series. A linear trend slope, w, is then calculated from this point to 2100. The standard deviation of the CESM-LENS natural run (Table 2.1), corresponding to the same region, is then calculated to determine σ, the natural SSTA variability. This value is then multiplied by two in order to have bounds at 95% of the natural variability, assuming a normal distribution. The following gives the time of emergence (ToE) in units of years from the starting year of the w calculation:

$$\text{ToE} = (2 \cdot \sigma)/w. \tag{2.4}$$

This ensures that the linear trend exceeds 95% of the natural variability assuming normal

distribution. The time of emergence is then the ToE calculated in (2.4) and added to the starting year of the w calculation.

2.3.4 Extended Empirical Orthogonal Function Analysis

An EOF analysis is a statistical method in which a dataset (varying in space and time) is decomposed into a set of statistical modes, consisting of uncorrelated simultaneous time series' (PC) and accompanying spatial patterns (EOF pattern). The percentage of total variance, R_i^2, that a mode represents can be found by dividing its associated eigenvalue, λ_i, by the sum of all eigenvalues and multiplied by 100,

$$R_i^2 = \frac{\lambda_i}{\sum_i \lambda_i} \times 100\%. \tag{2.5}$$

The largest eigenvalue corresponds to the mode that explains the most variability. The standard EOF analysis (e.g. *Deser et al.* (2010); *Loder and Wang* (2015, 2019)) is for a single dataset e.g. a single record of temperature at each spatial location. In order to perform an EOF analysis on a combined dataset where multiple records of temperature exist for each location, an EEOF approach was taken. Regionally-averaged SSTA from each region of interest (Fig. 2.2), with the linear trend removed, were calculated for each of the observation-based datasets (Table 2.1) according to a climatology from 1920 to 1950.

The combined dataset, T, can be written as

$$T(r,d,t) = \begin{bmatrix} T1(r,t) & T2(r,t) & T3(r,t) & T4(r,t) & T5(r,t) \end{bmatrix}, \tag{2.6}$$

consisting of a concatenated array of five different temperature datasets, $T1, T2, ...T5$, (See Table 2.1) where r is the region, d is dataset number ($d = 1, 2, ...5$), and t is time. Prior to the EEOF analysis, the detrended SSTA was also scaled by the area of the gridcell to account for the changing area between the regions of interest and the non-constant spacing in latitude; this has the additional effect of weighing each dataset equally. An

EEOF was then calculated on this array from January 1901 to December 2010, with the output being rescaled by the grid cell area. This analysis provides one PC time series and five EOF spatial patterns for each mode. The PC for each mode is divided by, and the EOF patterns for that mode are multipled by, the standard deviation of the associated PC so that the PCs are normalized to have a standard deviation of 1. All of the EOF modes can then be interpreted in units of $^{\circ}C$, assuming a PC value of order 1.

In order to determine whether each mode's explained variance is greater than random noise, modes generated from random data were compared to our results (also known as the Monte Carlo method; *Overland and Preisendorfer* (1982)). Covariance matrices and eigenvalues are determined for randomly generated arrays with a mean of 0 and unit variance. The eigenvalues are then divided by the total sum of eigenvalues in order to determine the percentage of explained variance. This process is then repeated 100 times. All percentages corresponding to the first mode across the 100 randomly generated arrays are then sorted from greatest to least. The same process is done for all remaining modes. The percentages resulting from the actual data products were then divided by the 95^{th} highest percentage of the same mode in the randomly generated arrays. This is known as the Rule N (*Overland and Preisendorfer*, 1982),

$$\text{Rule N} \quad = \quad \frac{R^2_{r,i}}{R^2_{N95,i}}, \tag{2.7}$$

where R^2 is the percentage of explained variance, r refers to the real mode derived from the SSTA datasets, N refers to modes derived from generated noise, and i represents the mode of interest. The superscript 95 represents the 95^{th} highest explained variance corresponding to a specific mode, i. Modes with Rule N values higher than 1 are considered significant and modes with Rule N values below 1 are considered indistinguishable from eigenvalues generated from noise.

It is important that the EEOF results have uncertainty estimates in time and space. The

five EOF patterns correspond to each of the observation-based datasets. The i^{th} space-time temperature pattern T_i can be written as

$$T_i(r,d,t) = p_i(r,d)u_i(t), \tag{2.8}$$

where T_i is the SSTA mode of variability, p_i is the EOF pattern, and u_i is the PC time series. A mean ($\overline{p_i}$) and standard deviation (σ_p) EOF pattern was found by spatially interpolating each of the EOF patterns to the common highest resolution and calculating the mean and standard deviation across the EOF patterns.

In order to convert the standard deviation in the EOF pattern to a standard deviation in the PC time series, the following method was used. If I rewrite the EOF pattern (p_i) as the sum of the mean pattern ($\overline{p_i}$) +/- the standard deviation (σ_{p_i}), then the uncertainty in $T_i(r,d,t)$, expressed as a standard deviation denoted $\sigma_{T_i}(r,d,t)$, can be determined using the following equation,

$$T_i(r,d,t) \pm \sigma_{T_i}(r,d,t) = (\overline{p_i}(r,d) \pm \sigma_{p_i}(r,d))u_i(t), \tag{2.9}$$

where $\sigma(\cdot)$ and $\bar{\cdot}$ are the standard deviation and the mean of the variable, respectively across all d (datasets). I follow this with a series of algebraic manipulations to determine a PC time series uncertainty σ_{u_i},

$$\begin{aligned} T_i(r,d,t) \pm \sigma_{T_i}(r,d,t) &= \overline{p_i}(r,d)u_i(t) \pm \sigma_{p_i}(r,d)u_i(t) && (2.10)\\ &= \overline{p_i}(r,d)\left(u_i(t) \pm \frac{\sigma_{p_i}(r,d)u_i(t)}{\overline{p_i}(r,d)}\right) && (2.11)\\ &= \overline{p_i}(r,d)(u_i(t) \pm \sigma_{u_i}(t)), && (2.12) \end{aligned}$$

where the standard deviation of the PC time series $\sigma_{u_i}(t)$ is given by

$$\sigma_{u_i}(t) = \frac{\sigma_{p_i}(r,d)u_i(t)}{\overline{p_i}(r,d)}. \tag{2.13}$$

2.4 Results

2.4.1 SSTA Time Series

Regionally-averaged SSTA time series (including linear trend) for the Northwest Atlantic were created for each of the regions of interest (Fig. 2.3). The SSTA time series include CESM-LENS (Fig. 2.3, grey and blue) and observation-based datasets (Fig. 2.3, red). Observation-based regionally-averaged SSTA time series from the Southern Mid-Atlantic Bight to the Northern Scotian Shelf (regions 1-7) show a clear multidecadal oscillation along with a noticeable steady increase after the year 2000. The CESM-LENS mean SSTA from the Southern Mid-Atlantic Bight to the Eastern Gulf of Maine (regions 1-4) stays within $\pm 2^{\circ}C$ from 1850 until 2000. CESM-LENS SSTA from the Western Gulf of Maine to the Northern Scotian Shelf (regions 5-7) have a large negative SSTA tail at the beginning of the time series (1920), and show a clear multidecadal oscillation. After 2000, the CESM-LENS mean SSTA from the Southern Mid-Atlantic Bight to the Northern Scotian Shelf (regions 1-7) increases steadily for the rest of the time series. This increase is mirrored in the observation-based dataset SSTA as far as the records allow.

Similarly in the Gulf of St. Lawrence, Grand Banks, and Flemish Cap (regions 8-11), both the observation-based datasets and CESM-LENS mean SSTA stay between $\pm 2^{\circ}C$ from 1850 to 2000. The multidecadal oscillation is less prevalent in the observation-based datasets in the Gulf of St. Lawrence, Grand Banks, and Flemish Cap (regions 8-11) as compared to the area from the Mid-Atlantic Bight to the Scotian Shelf (regions 1-7). After 2000, the Gulf of St. Lawrence, Grand Banks, and Flemish Cap (regions 8-11) show a steady increase in SSTA for the rest of the time series.

The Northern Newfoundland Coast and Labrador Shelf (regions 12-14) show little

multidecadal oscillation in both the observation-based dataset and CESM-LENS mean SSTA. The CESM-LENS mean SSTA is also consistently negative and differs from the observation-based datasets SSTA between 1900 and 2000 by roughly $1°C$. After the CESM-LENS mean SSTA plateaus around 1975, it undergoes a steady increase until the end of the time series.

Along the slope (regions 15-21), the observation-based datasets SSTA again shows a clear multidecadal oscillation. In the mid-slope (regions 17-19), the CESM-LENS mean SSTA is negative at the beginning of the time series, similar to the Western Gulf of Maine and Scotian Shelf (regions 5-7). After 2000, CESM-LENS mean SSTA undergoes a steady increase until the end of the time series.

2.4.2 Time of Emergence and Long-term Trend

Both the CESM-LENS mean and global gridded data product SSTA surpass the 95% bounds of natural variability in every region of interest over the time period of interest (Fig. 2.3). The natural bounds set by the standard deviation are smaller in the Northern Newfoundland and Labrador coastal regions (regions 12-14; 0.31-0.42°C) when compared to the southern shelf (regions 1-11; 0.39-0.63°C) and slope (regions 15-21; 0.43-0.69°C).

All of the regions of interest have a time of emergence that occurs before the year 2100 (Fig. 2.3, dashed lines). Along the southern shelf (regions 1-11), ToE occurs between 2023 and 2064 as is expected from the observed sharp increase in CESM-LENS mean SSTA after 1970. For the Northern Newfoundland and Labrador coastal regions (regions 12-14), ToE occurs between 2072 and 2091. This is the result of slightly negative CESM-LENS mean SSTA until around 2025. The cumulative sum of the SSTA gradient therefore does not surpass zero until much later in the time series when compared to regions where the CESM-LENS mean SSTA stays close to zero.

The long-term trend is approximately the same for most of the regions of interest outside of the Gulf of St. Lawrence and slope region 21 (Fig. 2.4). The increase in slope in the Gulf of St. Lawrence mirrors the relatively sharper increase seen in the SSTA time series

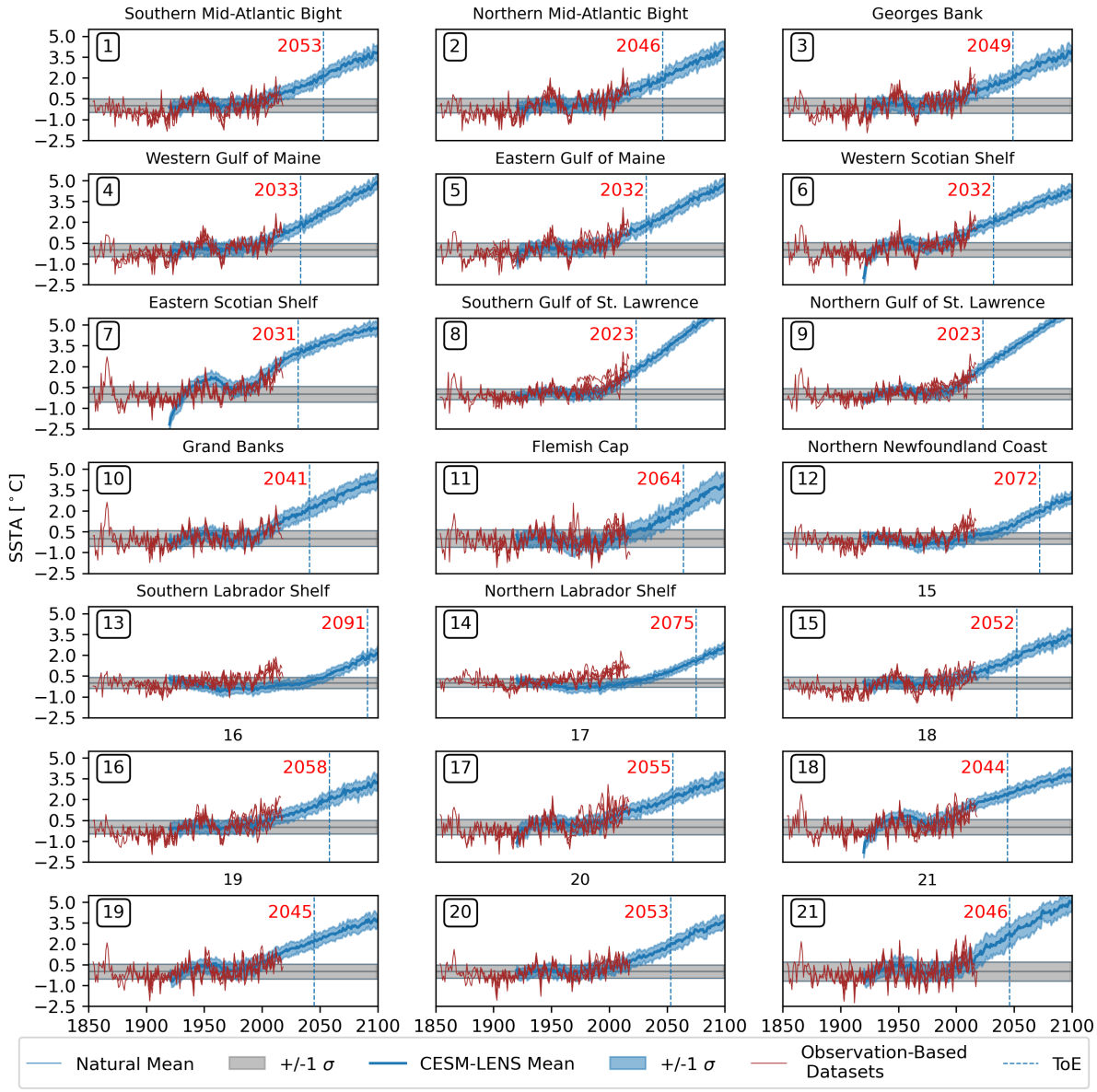

Figure 2.3: Annual mean SSTA time series for Northwest Atlantic shelf and slope regions of interest. SSTA time series are shown for global data products *(red lines)*, global climate model output historical and future run SSTA and standard deviation *(blue line and blue shaded area respectively)*, and global climate model output natural run mean and standard deviation *(black line and grey shaded area respectively)* are plotted from 1854 to 2100. The time of emergence (ToE) for the global model output historical and future runs is also shown *(dashed blue line and red text)*. The specific region that a time series represents is given in the top left corner.

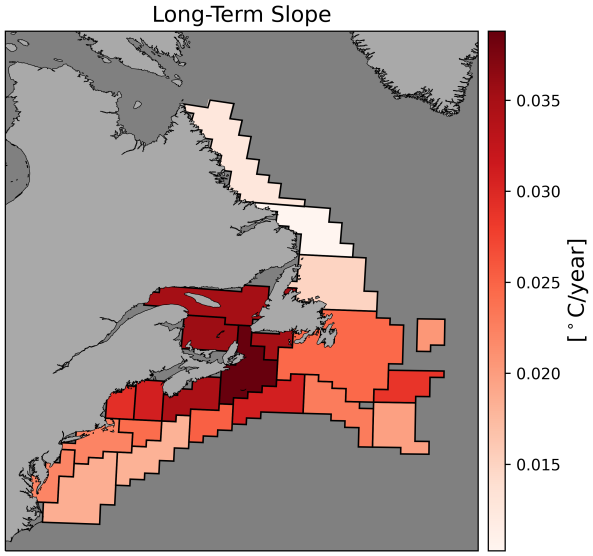

Figure 2.4: CESM-LENS SSTA slope calculated over the entire time series (1920-2100) for each of the regions of interest. The units are in $°C/year$.

(Fig. 2.3). The difference between the linear and a polynomial regression calculated from the beginning of the climate change signal to the end of the time series is relatively small implying that the use of a linear regression does not significantly influence the resulting time of emergence.

2.4.3 EEOF Patterns and Time Series

An EEOF was performed on detrended regionally-averaged SSTA from each of the observation-based datasets between 1901 and 2010. Using the method derived by *Overland and Preisendorfer* (1982), the first three EEOF modes were found to be significant (Fig. 2.5). Modes one through three explain 58.08%, 18.24%, and 6.07% respectively; collectively explaining 82.39% (Fig. 2.5).

Results from the multi-dataset EEOF show similar EOF patterns for all the data products (see Appendix A). Differences between the EOF patterns occur in the magnitude of the poles with ERSST showing the highest magnitude EOF consistently through the first three modes. The spatial correlation coefficient across datasets was calculated for each mode. EEOF modes one through three had a correlation coefficient range of 0.87-0.97, 0.93-0.98,

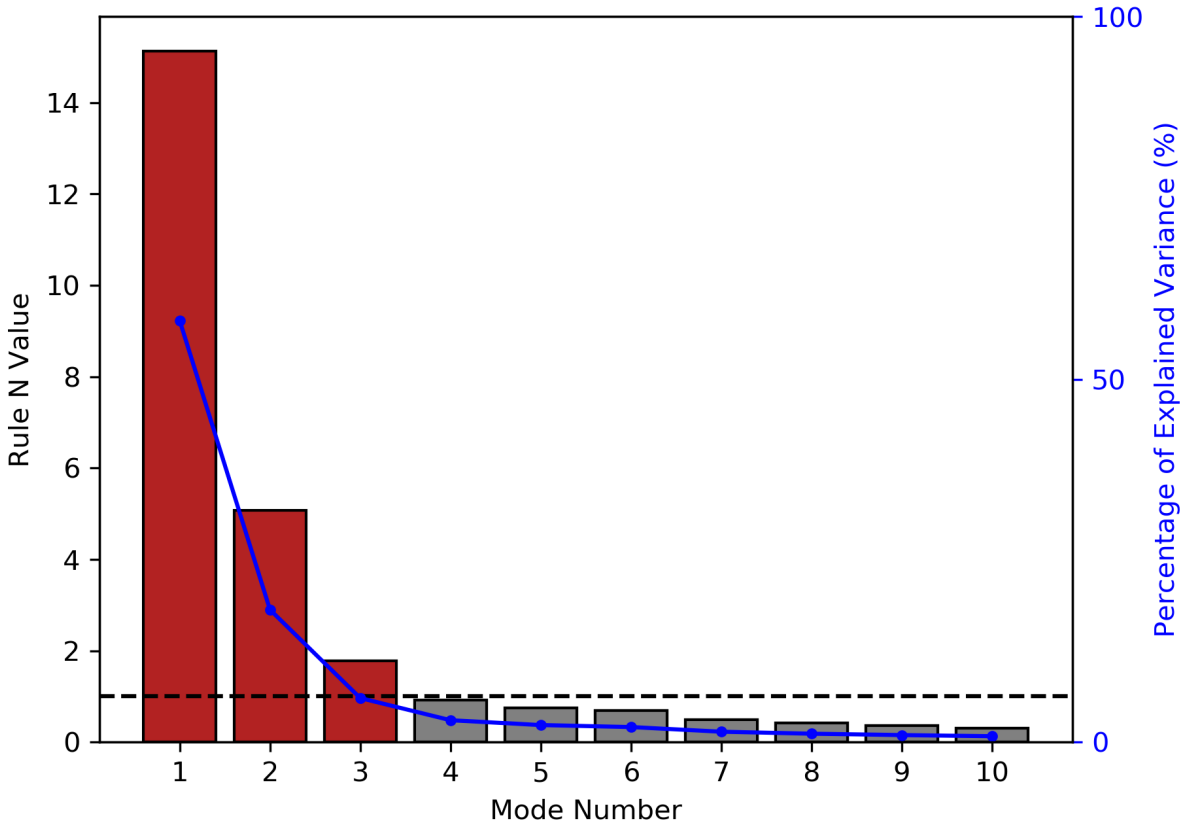

Figure 2.5: EEOF mode significance for the first ten modes using the methods derived by *Overland and Preisendorfer* (1982). The threshold of 1 for the Rule N determines significance in the first ten modes (*dashed black line*). Modes that are significant are coloured red and modes that are insignificant are coloured grey. The percentage of explained variance for the first ten modes is also shown (*blue line*).

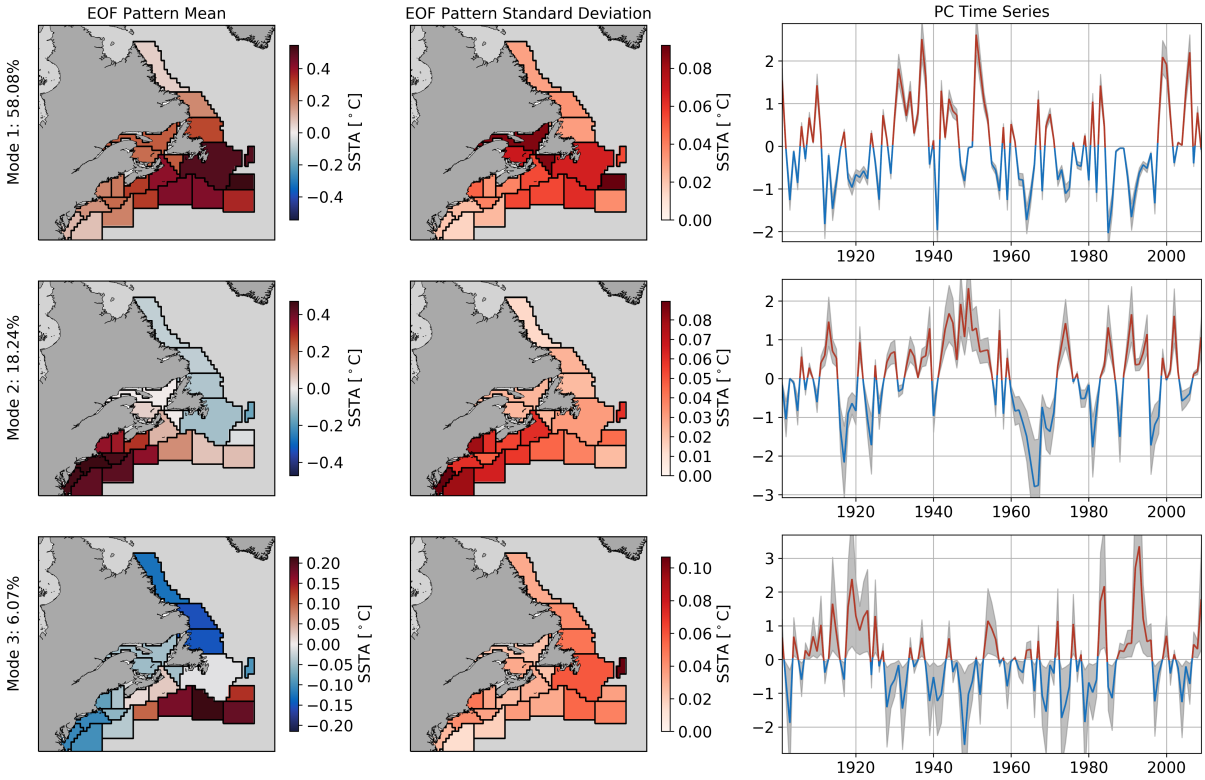

Figure 2.6: EOF spatial pattern mean and standard deviation (*first and second columns respectively*) and PC time series (*right column*). The EOFs and PCs correspond to the leading three modes (the rows) from the yearly detrended SSTA EEOF between 1901 and 2010. Positive PC years are shaded in red and negative PC years are shaded in blue, with gray shading showing ± 1 standard deviation to represent PC uncertainty in each of the modes. The percentage of explained variability is given in the y axis label of the EOF pattern mean.

and 0.77-0.98 respectively. This gives us confidence to combine the EOFs across datasets as described in Section 2.3.4. The EOF patterns were combined, the EOF pattern mean and standard deviation were determined, and the PC standard deviation was also determined (Fig. 2.6). Note that since the PC time series were normalized to have a standard deviation of 1, the EOF patterns can be interpreted as the SSTA response in °C to typical values of the PC time series.

EOF mean pattern 1 (Fig. 2.6, first row) has a positive sign throughout the area of interest with a positive pole located east of Newfoundland (regions 10,11,21) with a maximum 0.54°C. The mode decays to the north and south, over the Labrador Sea and Scotian Shelf,

Original Time Series		
Mode Number	AMO	NAO
1	0.61±0.01	0.03±0.02
2	0.01±0.03	0.29±0.04
3	-0.16±0.06	0.22±0.06
10 year Running Average Time Series		
Mode Number	AMO	NAO
1	0.77±0.02	-0.01±0.03
2	0.33±0.05	0.41±0.07
3	-0.34±0.11	0.48±0.09

Table 2.2: Correlation coefficients at 0 lag between the AMO and NAO index time series from 1901 to 2010 with the original and 10 year running average PC time series. Correlation coefficients were determined for the first three modes.

away from the main pole. PC 1 shows consistent multidecadal variability with minimums around 1915 and 1980 and maximums around 1940 and 2000. The first mode represents 58.08% of total detrended SSTA variability. Standard deviation between EOFs is largest at the centre of the pole with a maximum of 0.09°C. The highest temporal standard deviation in PC 1 is seen at the maximums and minimums previously stated. Even when considering the standard deviation, values for the first mode are significantly different from zero.

Correlation coefficients were determined between the AMO and PC1 over a shared time period, first using the original time series' and then with 10 year running average time series (Table 2.2). The PC1 uncertainty, calculated using the combined dataset, was used to add randomly generated white noise to the mean PC1, also known as a parametric bootstrap. This process was repeated 100 times allowing us to find a mean and standard deviation of the correlation coefficient. AMO and PC1 have a correlation coefficient of 0.61±0.01. 10-year filtered AMO and PC1 have a correlation coefficient of 0.77±0.02. The first mode shows resemblance to the first mode presented in *Loder and Wang* (2015), which they also correlated to the AMO. PC1 and NAO have a lower correlation coefficient of 0.03±0.02 for the original time series and -0.01±0.03 for the filtered time series.

EOF mean pattern 2 (Fig. 2.6, second row) has a slight negative pole east of Newfoundland and Labrador (regions 10-14) with a minimum of -0.03°C and a positive pole in the Mid-Atlantic Bight (regions 1-6, 14-16) with a maximum of 0.47°C. Maximums in spatial standard deviation are seen around the positive pole but are always less than the magnitude of the pole, therefore implying significance. PC2 again shows dominant multidecadal variability with the highest standard deviations being located at peaks and troughs. Troughs occur around 1915, 1960, and 1980 and peaks occur around 1950 and 2000, the same years where they occur for PC1. The second mode represents 18.24% of total detrended SSTA variability. The highest temporal standard deviation in PC2 is again seen at the maximums and minimums but with larger bounds compared to PC1. Mode 2 looks to have similar multidecadal variability as mode 1, but with additional higher-frequency variability. NAO and PC2 have a correlation coefficient of 0.29$\pm$0.04. Filtered NAO and PC2 (through a 10 year running average) have a correlation coefficient of 0.41$\pm$0.07. PC2 and AMO have a lower correlation coefficient of 0.01$\pm$0.03 for the original time series and 0.33$\pm$0.05 for the filtered time series.

EOF mean pattern 3 (Fig. 2.6, third row) has a positive pole in the eastern slope (regions 17-21) with a maximum of 0.22°C and two negative poles; one located in the Mid-Atlantic Bight (regions 1-4, 14) with a minimum of -0.12°C and one east of Labrador (regions 12-14) with a minimum of -0.15°C. PC3 shows similar multidecadal variability to PC2 and PC1 with maximums and minimums around the same time. The third mode represents 6.07% of the total detrended SSTA variability. The standard deviation in PC3 is consistently as large as the mean PC. Therefore, despite the significance found using the Rule N, I do not consider it a strong signal and so further analysis will not be performed on the third EEOF mode.

2.4.4 Heat Flux

The first two EEOF modes are now compared with regional ocean/atmospheric forcing variables. Positive correlation coefficients between PC1 and Q_{SW}, Q_{LW}, and Q_S are seen

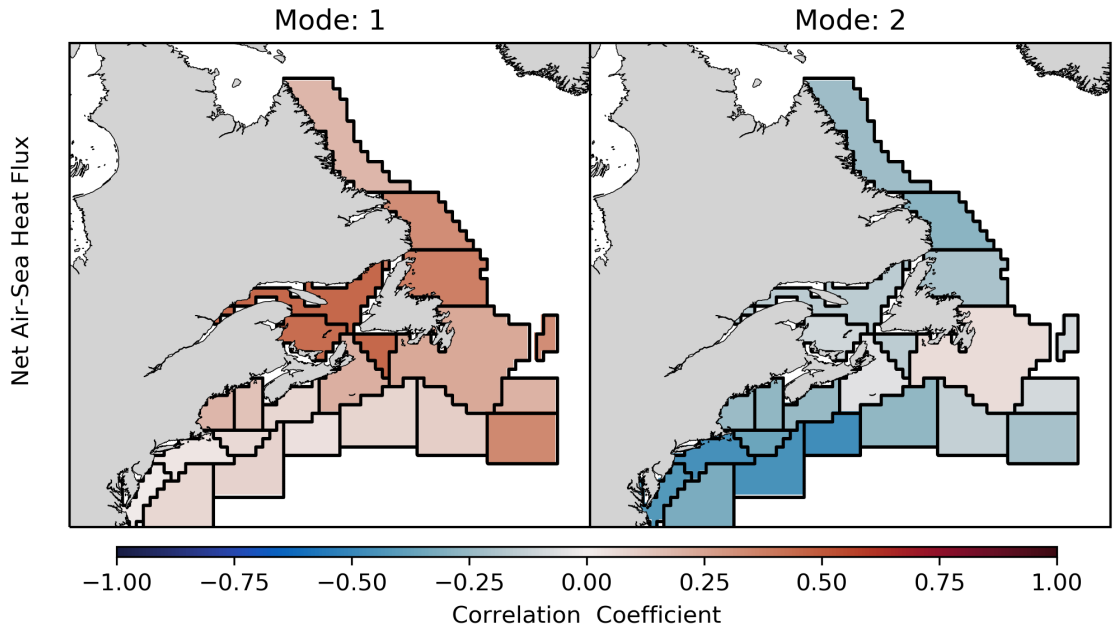

Figure 2.7: Correlation coefficient between the mean PC time series for modes 1 (left column) and 2 (right column), with total air-sea heat flux anomaly (Q_{NET}) from 1901 to 2010. Each region of interest is outlined in black and correlation coefficients are constant within each region.

in most areas of interest. Q_L and PC1 have a close-to-zero correlation coefficient in most regions (excluding the Gulf of St. Lawrence). Q_{NET} and PC1 have positive correlation coefficients in all areas of interest (Fig. 2.7).

Negative correlation coefficients are present along the Labrador Coast (regions 12-14) between PC2 and Q_{SW}. Positive correlation was found at all other regions. Negative correlation coefficients were found between PC2 and Q_{LW}, Q_S, Q_L and net heat flux in most regions. Q_{NET} and PC2 have a negative correlation in most regions of interest, including along the Labrador Shelf.

2.4.5 Freshwater Flux and Salinity

Results from the two leading EEOF modes were compared with freshwater flux, surface salinity, and depth-averaged salinity. Positive correlation is present for most regions (exluding regions 20, 21) between PC1 and freshwater flux. Negative correlation is present between PC1 and surface salinity from the Northern Scotian Shelf to the Southern Labrador

Shelf (regions 7-13; Fig. 2.8c). Depth-averaged salinity and PC1 have a positive correlation at all regions (excluding regions 8,12,13; Fig. 2.8e).

Freshwater flux and PC2 have a weak negative correlation at all regions excluding from the Gulf of Maine to the Flemish Cap (regions 4-11) where correlation is close-to-zero. Surface salinity and PC2 have a positive correlation from the Mid-Atlantic Bight to the Gulf of Maine, Gulf of St. Lawrence, Northern Newfoundland Coast, and Southern Labrador Shelf (regions 1-5,8,9,12,13). Negative correlation was found in the Northern Scotian Shelf (region 7) and slope regions 17-20 (Fig. 2.8d). All other regions are close-to-zero. Depth-averaged salinity and PC2 correlation coefficients have a similar spatial pattern to surface salinity and PC2 (Fig. 2.8f).

2.4.6 Ocean Currents and Wind

Results from the first two EEOF modes corresponding to the AMO and NAO indicies respectively were compared with surface ocean velocity, depth-averaged ocean velocity, and surface wind velocity. PC1 and surface ocean current correlations (Fig. 2.9a) follow the coastline and are directed northwards. Depth-averaged velocity follows a very similar pattern but with weaker correlation in southern slope and shelf regions (1-5, 15, 19, 20; Fig. 2.9c). PC1 and surface wind velocity correlations are directed approximately northwest in all regions of interest (Fig. 2.9e). Along the Labrador Coast, the correlation is directed parallel to the coastline in the northward direction.

PC2 and surface ocean velocity correlations (Fig. 2.9b) are directed in the southeast direction in northern regions of interest (regions 10-14). In southern regions of interest, the correlation is directed in the northeast direction (regions 1-6, 15, 16). Both correlations collide south of Newfoundland in the slope regions where the correlation is directed east. Depth-averaged velocity and surface wind velocity correlation patterns with PC2 follow a similar spatial pattern to the correlation between surface ocean velocity and PC2.

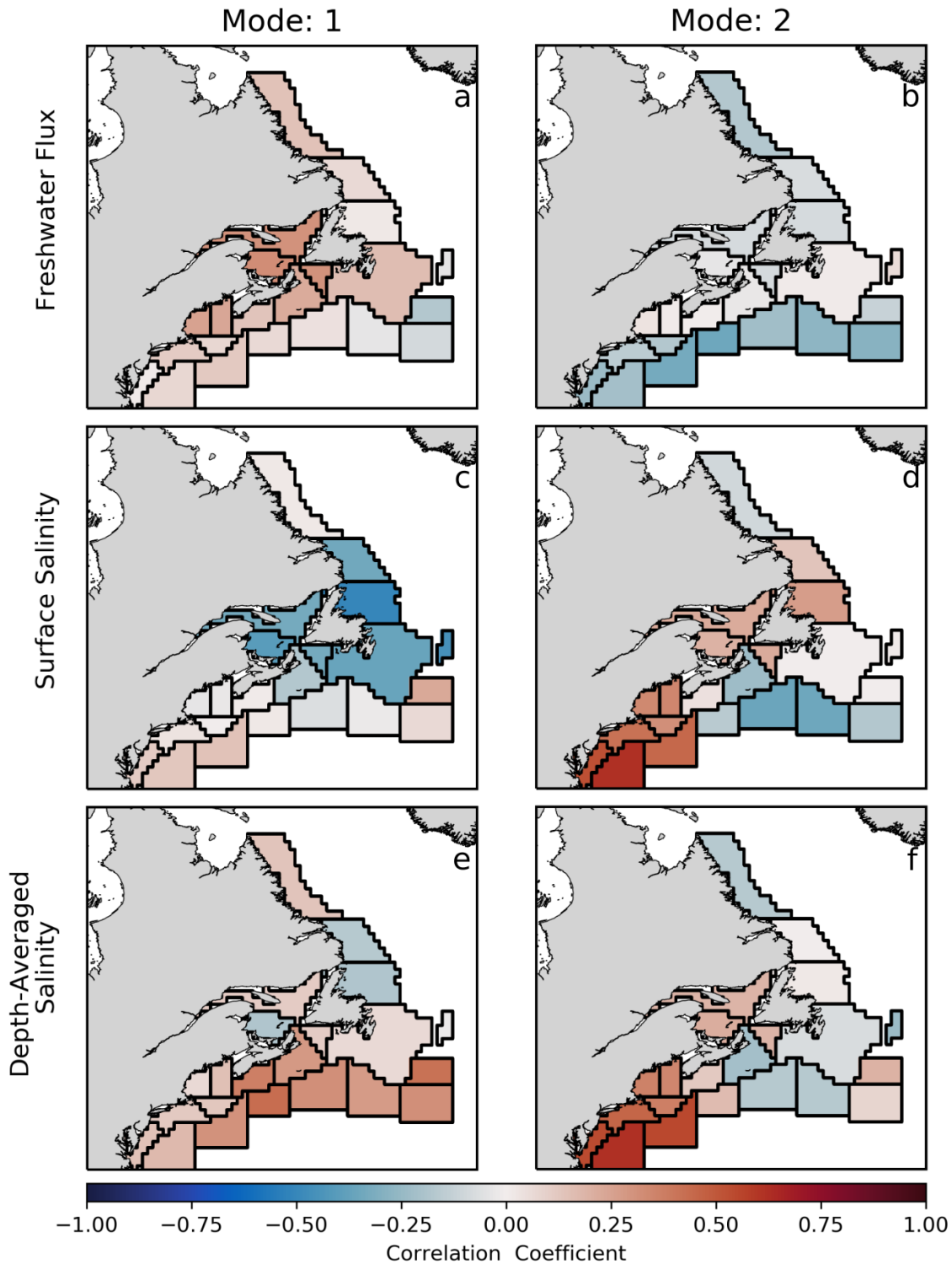

Figure 2.8: Correlation coefficient between the mean PC time series 1 and 2, with freshwater flux anomaly, surface salinity anomaly, and depth-averaged salinity anomaly from 1901 to 2010. Each of the variables has also been linearly detrended. Each region of interest is outlined in black and correlation coefficients are constant throughout.

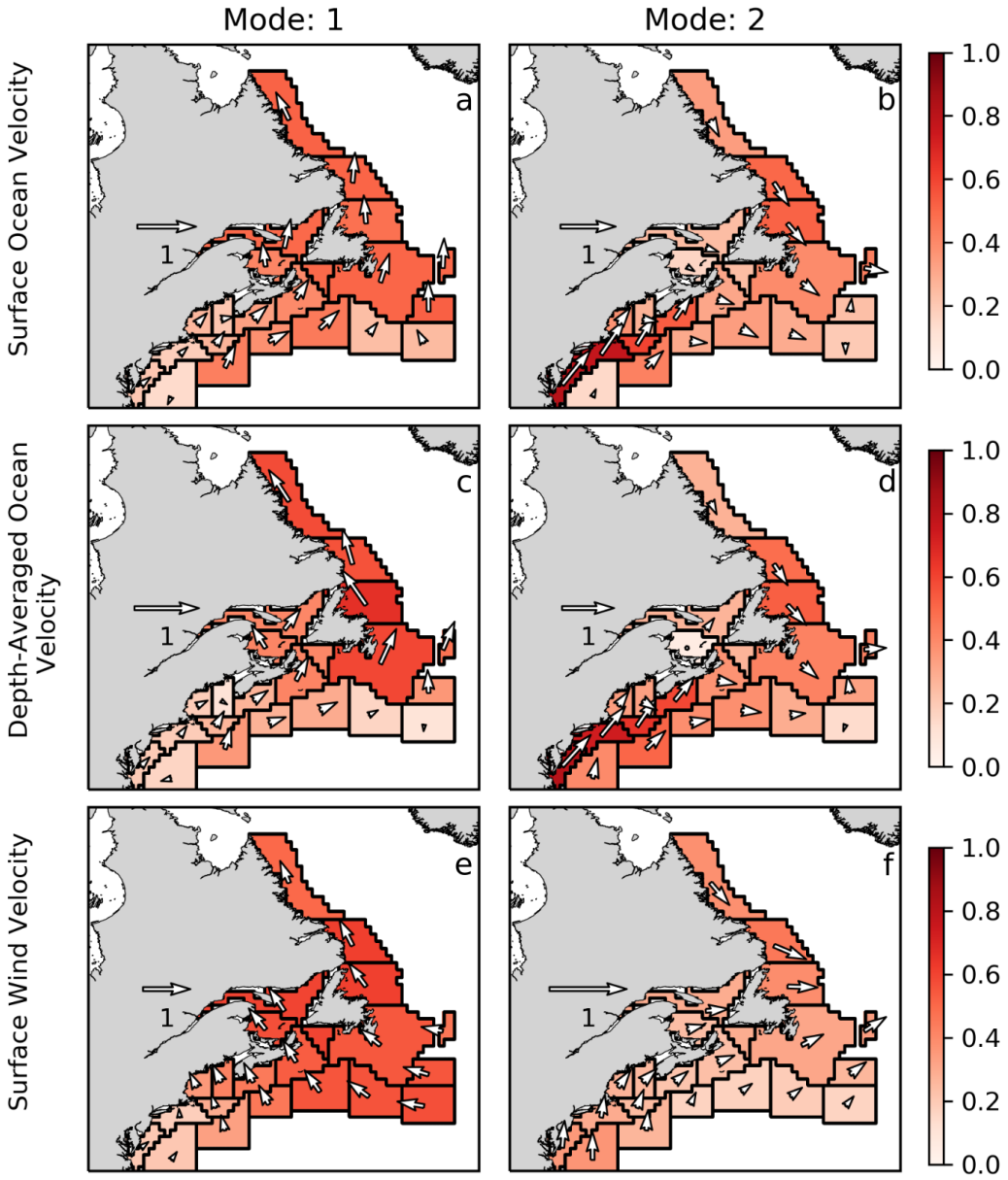

Figure 2.9: Correlation coefficient between the mean PC time series 1 and 2, with surface oean velocity anomaly, depth-averaged ocean velocity anomaly, and surface wind velocity anomaly from 1901 to 2010. Each of the variables has also been linearly detrended. Each region of interest is outlined in black and correlation coefficients are constant throughout. The unit correlation arrow is given in each plot. The arrows were calculated by summing the zonal and meridional correlation coefficients for each region.

2.5 Discussion

The SSTA is now analyzed in shelf and slope regions of the Northwest Atlantic from Cape Hatteras, North Carolina (35°N), to Cape Chidley, Labrador (60°N) using multiple observation-based datasets and global model outputs. Long-term increases in SSTA have been identified in all regions of interest under the RCP 8.5 emissions scenario. The time of emergence of anthropogenic warming past the range of natural variability for each region of interest was determined. Annual to multidecadal variability in SSTA has been isolated using a novel EEOF method which considers cross-dataset variability. The dominant modes have been linked to known climate modes (AMO, NAO) and regional atmospheric/oceanic forcing variables. The correlation coefficients between PC time series and oceanic/atmospheric variables have been determined to better understand the physical forcing behind multidecadal SST variations in the Northwest Atlantic. Evidence is found to support previous studies findings linking the AMO and NAO to the Northwest Atlantic. It can be seen that it may extend to the shelf and slope regions as well.

Time of emergence along the Labrador Shelf (2072-2091) (Fig. 2.3) were later than regions in the Scotian Shelf and Gulf of Maine (2031-2033). This is most likely due the steady negative mean SSTA from 1920 to 2025 and less prominent multidecadal oscillation along the Labrador Shelf. SSTA multidecadal variability in the Labrador Sea closely mimics NAO but long-term SSTA records along the Labrador Shelf are rare (*Alexander and Deser*, 1995; *Petrie*, 2007; *Deser et al.*, 2010). Despite this, *Chen et al.* (2020) noted slow, steady warming and less oscillation in SSTA between 1982 and 2018. The absence of multidecadal oscillation in the Labrador Shelf could disallow the possibility of "stalling" anthropogenically-induced SST warming like is seen in other regions of the Northwest Atlantic (*Loder and Wang*, 2015). This could make SSTA in the Labrador Shelf especially susceptible to anthropogenically-induced climate change. It is important to note that large cross-dataset variability in SSTA is noted in the Labrador Sea as a result of data sparsity

(*Deser et al.*, 2010; *Loder and Wang*, 2015, 2019).

Excluding the Gulf of St. Lawrence and Labrador Shelf, all shelf regions show a clear multidecadal oscillation between 1900 to 2010. An abrupt increase in CESM-LENS historical and future mean SSTA is also present from 2000 to 2100. Multidecadal oscillation in the form of AMO and NAO has been well documented from the Mid-Atlantic Bight to the Scotian Shelf, the Grand Banks, and the Flemish Cap over the last century (*Deser et al.*, 2010; *Loder and Wang*, 2015, 2019). *Chen et al.* (2020) noted positive trends in SSTA for the slope and shelf regions of the Northwest Atlantic between 1982 and 2018. Relatively lower trends were recorded in the Gulf of St. Lawrence.

Considering projected model outputs until 2100, it is clear that despite the presence of large-scale multidecadal oscillation in many regions, SSTA still tends upwards past natural bounds at a steady rate. This sustained divergence from the bounds of natural variability can be attributed to projected anthropogenic emissions under the RCP 8.5 "business as usual" emissions scenario (*Kay et al.*, 2015). Assuming that greenhouse gas emissions continue to follow the RCP 8.5 emissions scenario, SSTA can be expected to increase beyond bounds of natural variability in all regions of interest over the next 80 years.

I now present a conceptual model for the formation of an AMO event, and its expression in shelf SSTA (fig. 2.10). The formation of a positive AMO event occurs when negative air-sea heat flux anomalies in the Labrador Sea drive Atlantic Meridional Overturning Circulation to advect warm waters north (*Wills et al.*, 2019). This leads to a warming of subpolar waters after several years. Surface and depth-averaged ocean velocity anomalies correlated with the PC1 highlight this, showing a strengthened Gulf Stream and weakened Labrador Current (Fig. 2.9, Mode: 1). Consistent positive NAO years create negative heat fluxes in the Labrador Sea (and by extension shelf) driven by strong westerly winds (*Wills et al.*, 2019) (Fig. 2.10a). This in turn enhances deep water formation and strengthens the Atlantic Meridional Overturning Circulation (Fig. 2.10b). Therefore consistent positive NAO years could potentially force positive AMO years after several years. Positive NAO

years do not have to occur continuously. Positive years as a result of white noise can also cause the formation of positive AMO events (*Wills et al.*, 2019).

Negative air-sea heat flux anomalies and westerly wind velocity anomalies seen in the Labrador Shelf Regions (Fig. 2.7, 2.9, Mode: 2) support the positive NAO index hypothesis. After a sufficient time, increased transport of warm water through the Atlantic Meridional Overturning Circulation, causes the formation of a low pressure cell in the Northwest Atlantic subpolar gyre driving warm air northwards. This leads to positive air-sea heat flux anomalies throughout the region (*Wills et al.*, 2019) (Fig. 2.7, Mode: 1) driven by south easterly winds (Fig. 2.9, Mode: 1). It is at this point that the positive AMO event reaches a maximum (Fig. 2.10c).

Total air-sea heat flux anomalies shows a positive correlation with PC1 throughout the Northwest Atlantic coast and shelf regions (Fig. 2.7, Mode: 1). The increase of air-sea heat flux into the Labrador shelf regions may increase stratification in the region eventually slowing down Atlantic Meridional Overturning Circulation (*Deser et al.*, 2010; *Wills et al.*, 2019). This will lead to a dissipation of the positive AMO event (Fig. 2.10d).

The spatial correlation coefficients between PC1 and depth-averaged salinity agree with increased advection of warm salty water through the Gulf Stream (excluding regions 7, 11, 12) (Fig. 2.8, Mode: 1). *Wills et al.* (2019) notes increased evaporation over the Labrador Sea region although that is not seen here. Surface salinity shows negative correlation with PC1 throughout most northern regions although this could possibly be due to local precipitation effects.

Correlations between the shelf modes shown here and regional ocean and atmosphere variables support the underlying mechanisms behind the formation of positive AMO index years brought forward by *Wills et al.* (2019). Restricting for the Northwest Atlantic shelf and slope regions does not noticeably change the governing mechanisms behind variations in PC1 when compared to the whole Northwest Atlantic.

Positive NAO years correspond to a strengthening of the low and high pressure cells

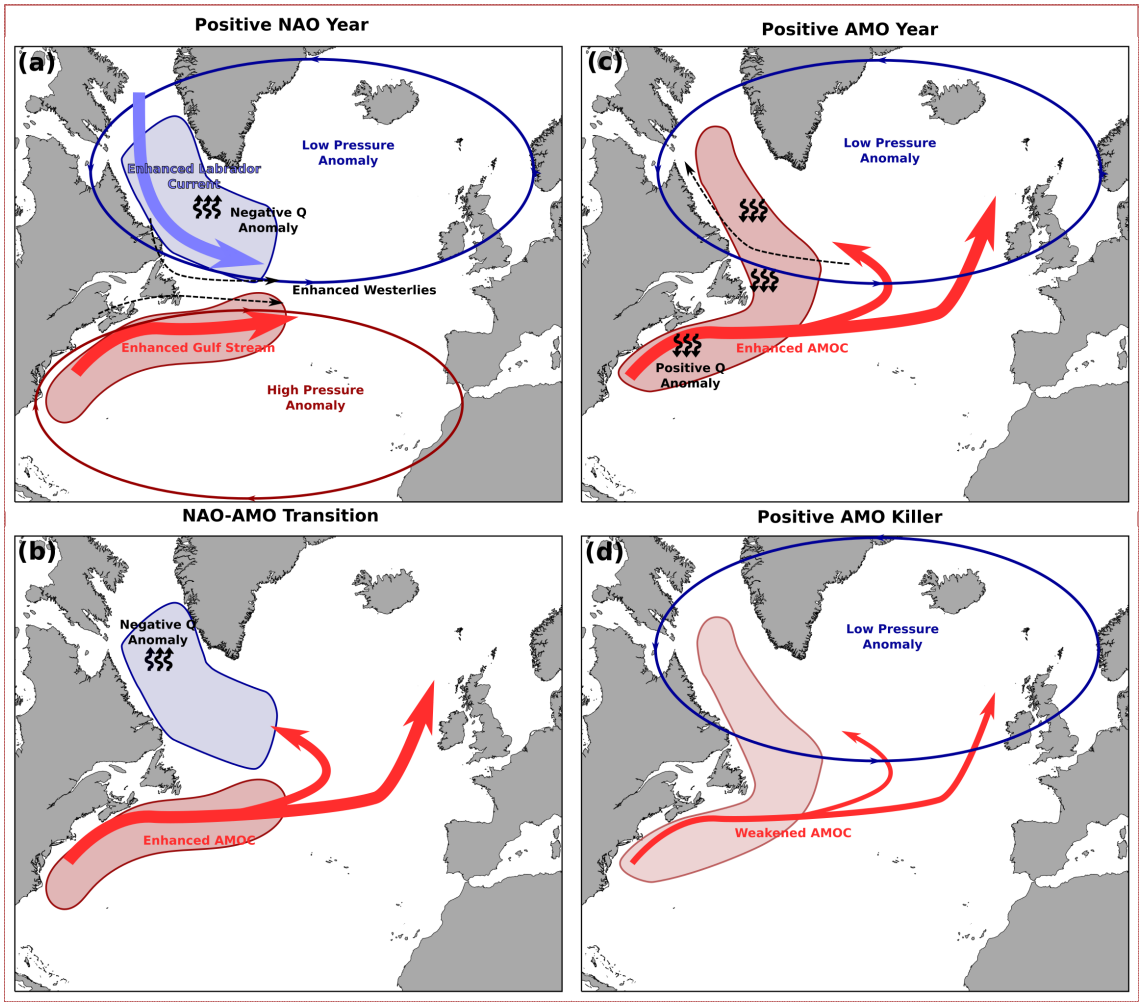

Figure 2.10: Schematic of the formation of a positive AMO event. The positive NAO year (a) enhances the Atlantic Meridional Overturning Circulation (AMOC) leading to an NAO-AMO transition (b). After sufficient time, a positive AMO year occurs (c) which is eventually killed by a weakened AMOC (d). Areas of positive (*red shaded area*) and negative (*blue shaded area*) SSTA are shown in each subplot.

centred around Iceland and the Azores respectively. This in turn changes wind velocity magnitude and direction (*Deser et al.*, 2010). Anomalous westerly winds positively correlate to PC2 in regions 8-13 (Fig. 2.9, Mode: 2). The persistent westerly winds drive the ocean to lose heat (Fig. 2.6) over the atmosphere resulting in a negative air-sea heat flux (Fig. 2.7, Mode: 2). This is supported by the negative correlation of Q_{NET} with PC2.

The mechanism by which the wind changes SST in the region is through Ekman Energy Fluxes. *Deser et al.* (2010), using similar wind velocities to those found here, showed that the resulting Ekman Currents along with latent and surface heat flux drove the di-polar structure seen in EOF2 (Fig. 2.6). The results of the Ekman Currents can be seen in the surface ocean velocity where the typical Labrador Current structure is magnified (Fig. 2.9, Mode: 2). A similar structure is found in the depth-averaged ocean velocity anomalies (Fig. 2.9, Mode: 2) but it is unclear whether this is driven exclusively by the anomalous Ekman Current. Increased cold water transport in the Labrador Shelf regions driven by Ekman Currents results in negative SSTA from the Grand Banks up to the Labrador Shelf (regions 9-13) (Fig. 2.6). A similar opposite result occurs with the magnified Gulf Stream, resulting in anomalously warm waters in the southern shelf and slope (regions 1-7, 15-20) (Fig. 2.6).

Diminished wind velocity anomalies correlated to PC2 (Fig. 2.9) in the southern shelf and slope (regions 1-8, 15-21) show less prominent westerlies therefore losing less heat to the atmosphere. *Deser et al.* (2010) notes anomalous easterly surface wind velocities at the mid-latitudes. The restraints in the spatial domain or spatial averaging could explain the lack of easterlies seen here.

With increased advection through the Labrador Current and Gulf Stream, I would expect to see negative surface salinity anomalies along the Labrador Shelf and positive surface salinity anomalies in the south. Mid-shelf, slope, and Labrador shelf regions do not support this hypothesis. It is possible that despite increased advection of warm salty water from the south and cold fresh water from the north, other processes result in the shown surface

salinity anomalies.

By using a novel EEOF analysis in combination with comparisons to atmospheric/oceanic variables, further evidence is provided to the proposed mechanism behind positive AMO event development. Furthermore, this has been done while considering SSTA cross-dataset variability and focusing on the slope and shelf regions of the Northwest Atlantic. Long-term SSTA time series have also been created for each of the regions of interest using multiple observation-based datasets and global climate model output. Using these time series, times of emergence have also been calculated.

It is important to consider multiple observation-based datasets when interpreting long-term SST trends and variability. Interpolation method, data sparsity, and corrections to the source data can alter the reported SST. Likewise, interpretation of EOF analysis over extended time periods should be performed with an EEOF and multiple datasets if available. The specific definition of what each observation-based dataset represents should also be taken into consideration. As noted previously, the depth, measurement method, etc. can differ between datasets resulting in different outcomes. Special care should be taken when comparing these products with one another. Research on Labrador Shelf SST multidecadal oscillation is rare due to a lack historical records. It is recommended that further research be done on historical SST variability and trends along the Labrador Shelf.

Given the very likely possibility of continued (and possible increase in) greenhouse gas emissions (*Bindoff et al.*, 2019), our results show that increases in SSTA will be seen throughout the Northwest Atlantic coast and shelf regions until at least 2100. With increases in SSTA along with multidecadal oscillation, extreme temperature events like those observed in 2012, are expected to increase (*Hobday et al.*, 2018; *Oliver et al.*, 2018).

Correlations between oceanic/atmospheric variables with EEOF PC time series allow us to determine possible physical forcings behind multidecadal variabiliy in the Northwest Atlantic shelf and slope regions. It is still impossible to say which of the comparison variables plays a more active role with just the use of correlation coefficients. I recommend

that a long-term heat budget equation be made for the regions of interest defined here in order to determine the relative contributions of different variables to SSTA variability.

CHAPTER 3

PHYSICAL FORCES BEHIND MODES OF VARIABILITY IN NORTHWEST ATLANTIC SURFACE TEMPERATURE TENDENCY

3.1 Introduction

It has been well established that a large percentage of coastal Northwest Atlantic SSTA variability can be attributed to defined modes of natural yearly-to-multidecadal variability (*Deser et al.*, 2010; *Loder and Wang*, 2015, 2019). In combination with the region's recent warming trend, this makes the area especially susceptible to extreme SST events (*Hobday et al.*, 2018; *Oliver et al.*, 2018). Given the historic and current environmental, cultural, and economic importance of the area, extreme SST events have the potential to have a large-scale coastal impact on local populations and ecosystems (*Mills et al.*, 2013). This underlies the importance of understanding the physical forcing behind, as well as being able to predict, modes of SST variability.

The AMO is a large-scale climate mode exhibiting multidecadal variability in SST on timescales of 60-70 years (*Deser et al.*, 2010; *Loder and Wang*, 2015). Positive (negative) AMO years are associated with a positive (negative) SSTA pole located in the middle of the North Atlantic (*Deser et al.*, 2010; *Loder and Wang*, 2015, 2019; *Wills et al.*, 2019).

Positive AMO years may occur as the result of consistent negative air-sea heat flux over the Labrador Sea driving Atlantic Meridional Overturning Circulation to advect warm water north (*Wills et al.*, 2019). This leads to anomalously warm ocean temperatures throughout the Atlantic and the formation of a low pressure cell. With time, the Atlantic Meridional Overturning Circulation over-corrects the initial cold water scenario leading to increased stratification in the Labrador Sea. This weakens the Atlantic Meridional Overturning Circulation and causes the dissipation of the positive AMO event. It should be noted that the physical forcings behind the AMO are still debated (*Deser et al.*, 2010; *Loder and Wang*, 2015). This is partially due to the long timescale on which the AMO oscillates and the corresponding lack of available data. Given that many of the oceanic/atmospheric variables needed to determine the forcing behind AMO changes are not observed over many AMO cycles (if any), this makes the analysis of potential forcing difficult.

The NAO represents changes in sea level pressure between the Arctic and the Atlantic subtropics forced by the redistribution of atmospheric mass (*Visbeck et al.*, 2003; *Marshall et al.*, 2001; *Deser et al.*, 2010). The effect of the NAO on North Atlantic SSTA is characterized as a tripolar structure, with negative anomalies in the subpolar North Atlantic and subtropics, and positive anomalies in the mid-latitudes (*Deser et al.*, 2010; *Loder and Wang*, 2015, 2019). The combined latent and sensible heat flux mirrors this tripolar structure and so the ocean loses heat energy to the atmosphere in the subpolar North Atlantic (*Deser et al.*, 2010). This is the result of the changes in sea level pressure, which during positive index years results in an strengthened Iceland low pressure cell and Azores high pressure cell. The strengthening of the pressure cells results in anomalously strong westerlies and northeast trade winds. Meanwhile, at mid-latitudes the ocean gains heat energy from the atmosphere as a result of weakened westerlies and enhanced warm air advection along the Eastern United States. Anomalous wind speeds and the resulting Ekman transport can also strengthen the Gulf Stream and Labrador Current during positive years (*Deser et al.*, 2010).

The physical forcing behind modes of mixed layer temperature variability along the Northwest Atlantic shelf and slope will be investigated here. This chapter uses the new Community Earth System Model version 2 - Large Ensemble (CESM2-LENS) output to create a spatially and temporally complete mixed layer temperature tendency anomaly heat budget of the Northwest Atlantic shelf and slope regions from 1850 to 2015. This will be done in the pursuit of better understanding the physical forcing behind the AMO and NAO climate modes over multiple cycles. Temperature tendency anomaly time series will be determined for predefined regions across all ensemble members. In order to determine the AMO and NAO indices, an EOF will be performed on each ensemble member. Heat budget terms for each of the regions, will then be averaged over positive (formation) and negative (dissipation) AMO and NAO years according to their corresponding ensemble member EOF results. Heat budget findings show that the observed AMO and NAO indices and SSTA spatial patterns are accurately reproduced in the CESM2-LENS output. A difference in the physical forcing behind AMO formation years was found in this chapter between the shelf and slope regions. Evidence was found that NAO formation years can lead to the formation of a positive AMO event. Lastly, it was found that NAO formation and dissipation years along the Northwest Atlantic shelf and slope are mainly driven by air-sea heat flux anomalies.

3.2 Data

Model output was used from the CESM2-LENS global climate model which was developed to examine climate sensitivity to anthropogenically-forced global warming (*Rodgers et al.*, 2021). The downloaded output of the CESM2-LENS (1850-2015) is subject to historical records of anthropogenic and natural forcing (*Rodgers et al.*, 2021). The ocean and atmosphere outputs are from the Parallel Ocean Program version 2 and have a non-constant spatial resolution of approximately 1° latitude by 1° longitude with latitude grid spacing increasing towards the poles. CESM2-LENS has 100 ensemble members consisting of

80 micro-initializations and 20 macro-initializations. The macro-initializations use 20 independent initialization dates at a ten-year interval between the years 1001 and 1191 from a pre-industrial reference simulation. Here, I use ten of the macro-initialization ensemble members due to lack of currently available data; 1001, 1021, 1041, 1061, 1081, 1101, 1121, 1141, 1161, and 1181. The following monthly ocean/atmospheric variables were obtained from the CESM2-LENS output; temperature tendency ($\frac{\partial T}{\partial t}$), mixed layer depth (MLD) (h), advective flux of heat in the grid-x, y, and z directions ($\nabla \cdot (\vec{v}T)$), total surface heat flux (Q_{SHF}), solar shortwave heat flux (Q_{SW}), temperature flux across the bottom face from diabatic implicit vertical mixing, sensible heat flux (Q_{sen}), upwards longwave heat flux and downwards longwave heat flux (sum to Q_{LW}), and finally the heat flux due to the latent heat of evaporation, melt, snow, and ice runoff (summed to the latent heat flux, Q_{lat}). MLD is defined as the shallowest depth where the local buoyancy gradient is at its maximum (*Large et al.*, 1997). It is important to note that the CESM2-LENS output produces an incorrect separation and path of the Gulf Stream and an unrealistically extensive sea ice coverage over the Labrador Sea (*Danabasoglu et al.*, 2020). Both of these error could have an effect on multidecadal SSTA variability in the Northwest Atlantic.

The observed monthly AMO index (1870 to 2015) and NAO index (1865 to 2019) was obtained from *Trenberth and Shea* (2006) and *Hurrell et al.* (2003) respectively. Both the AMO and NAO were averaged to annual means. For AMO and NAO indices derived from temperature tendency output, positive and negative years correspond to formation and dissipation years respectively. The AMO is defined as a coherent mode of natural variability that oscillates on a time scale of 60-70 years (*Trenberth and Shea*, 2006). The NAO describes the difference in sea level pressure between the Azores high pressure cell and Iceland low pressure cell (*Hurrell et al.*, 2003).

3.3 Methods

3.3.1 Regions of Interest

In order to determine the meridional and temporal structure of mixed layer temperature tendency anomaly in the Northwest Atlantic shelf and slope region, specific regions of interest (the same as those used in 2.3.1) were defined using local bathymetry following *Richaud et al.* (2016) and *Chen et al.* (2020). The regions extend meridionally from Cape Hatteras, North Carolina, to Cape Chidley, Labrador (Fig. 2.2). Regions 1-14 correspond to the Northwest Atlantic shelf (0 - 1000m depth). Regions 1-3 are associated with the Mid-Atlantic Bight, 4-5 with the Gulf of Maine, 6-7 with the Scotian Shelf, 8-9 with the Gulf of St. Lawrence, 10-11 with the Grand Banks and Flemish Cap, and 12-14 with the Northern Newfoundland Coast and Labrador Shelf.

Regions 15-21 correspond to the Northwest Atlantic slope (4000m+ depth) and are restricted to be south of 45°N as slope waters along the Labrador Shelf are difficult to define (*Chen et al.*, 2020). The slope regions also follow the general path of the Gulf Stream.

3.3.2 Statistical Decomposition of Temperature Tendency

Temperature can be considered the sum of three components:

$$T(t) = T^{\mathrm{Tr}}(t) + T^{\mathrm{s}}(t) + T^{'}(t), \tag{3.1}$$

where T is the temperature at time t, T^{Tr} is the linear temperature trend at time t, T^{s} is the temperature seasonal cycle at time t, and $T^{'}$ is the temperature anomaly at time t. Here, I am interested in tendency and so the derivative with respect to t is determined:

$$\frac{\partial T}{\partial t} = \frac{\partial T^{\mathrm{Tr}}}{\partial t} + \frac{\partial T^{\mathrm{s}}}{\partial t} + \frac{\partial T^{'}}{\partial t} \tag{3.2}$$

where $\frac{\partial T}{\partial t}$ is the temperature tendency at time t, $\frac{\partial T}{\partial t}^{\mathrm{T}r}$ is the linear trend of the temperature tendency at time t, $\frac{\partial T}{\partial t}^{\mathrm{s}}$ is the temperature tendency seasonal cycle (climatology) at time t, and $\frac{\partial T}{\partial t}^{'}$ is the temperature tendency anomaly at time t. The linear temperature tendency trend, $\frac{\partial T}{\partial t}^{\mathrm{T}r}$, was calculated by least square regression over the entire time period. The climatology, $\frac{\partial T}{\partial t}^{\mathrm{s}}$, calculated by finding the mean temperature tendency for each month from 1920 to 1950, was then subtracted from the temperature tendency along with the temperature tendency trend, to find the temperature tendency anomaly, $\frac{\partial T}{\partial t}^{'}$. This was repeated for each of the CESM2-LENS ensemble members.

3.3.3 Atlantic Multidecadal Oscillation and North Atlantic Oscillation

In addition to the observed AMO and NAO indices, indices from the CESM2 climate model were calculated as well. SSTA from the North Atlantic between the equator and 60°N was spatially averaged, and then smoothed with a 10-year running average. The global mean SSTA, between 60°N and 60°S, was then subtracted from the smoothed Atlantic SSTA to find the AMO index. The AMO index was derived following the methods of *Trenberth and Shea* (2006). The associated SSTA spatial pattern covers the entire North Atlantic and has a period of 60-80 years.

The CESM2 NAO index was derived from finding the difference in sea level pressure between Libson, Portugal (64.148°N and 21.935°W, represents the Azores high) and Reykjavik, Iceland (38.685°N and 9.255°W, represents the Iceland low), following *Hurrell et al.* (2003).

3.3.4 Empirical Orthogonal Function

Prior to the EOF analysis (see 2.3.4), the detrended mixed layer temperature tendency anomaly was scaled by the area of the gridcell to account for the changing area of the grid cell with latitude; this has the additional effect of weighing each region depending on the regions area. An EOF was then calculated from 1850 to 2015, with the output being

rescaled by grid cell area. The PC for each mode is divided by, and the EOF pattern for that mode is multipled by, the standard deviation of the associated PC so that the PCs are normalized to have a standard deviation of 1. All of the EOF modes can then be interpreted in units of $^{\circ}C/$month, assuming a PC value of order 1. This analysis provides one PC time series and one EOF spatial pattern for each mode. The process was repeated for each of the CESM2-LENS ensemble members. The original mixed layer temperature tendency anomaly time series, $\frac{\partial T}{\partial t}'$, can be recovered as the sum of all EOF spatial patterns multiplied by their corresponding PC time series,

$$\frac{\partial T'}{\partial t} = \sum_i \text{EOF}_i(x,y)\text{PC}_i(t), \tag{3.3}$$

where an individual mode can be written as,

$$\frac{\partial T_i'}{\partial t} = \text{EOF}_i(x,y)\text{PC}_i(t). \tag{3.4}$$

We can write this in terms temperature anomaly T', rather than tendency, by integrating with respect to time:

$$\text{d}T_i' = \text{EOF}_i(x,y)\text{PC}_i(t)\text{d}t, \tag{3.5}$$

$$\int_0^t \text{d}T_i = \int_0^t \text{EOF}_i(x,y)\text{PC}_i(s)\text{d}s, \tag{3.6}$$

$$T' - T_0' = \text{EOF}_i(x,y) \int_0^t \text{PC}_i(s)\text{d}s, \tag{3.7}$$

where T_0' is the temperature anomaly at time 0. We define our anomaly such that $T_0' = 0$. Then the integrated EOF decomposition can be written as,

$$T_i' = \text{EOF}_i(x,y)\text{CPC}_i(t), \tag{3.8}$$

where the cumulative PC time series for mode i, CPC_i, is equal to $\int_0^t \text{PC}_i(s)\text{d}s$ and has

units of s. The CPC was calculated for the first two modes so that, when multiplied by the EOF, a time series with units temperature rather than a temperature tendency, could be compared with the CESM2-derived and observed AMO and NAO indices.

Due to how the initial conditions are defined for CESM2-LENS ensemble members, namely that initial conditions are taken every ten years from a natural control run and therefore do not have constant phasing across ensemble members, it was found that the use of an EEOF (see Chpt. 2) was not practical for determining modes of variability from CESM2-LENS output. It was also found that temperature tendency time series are noisier than the temperature time series they are derived from. This makes the use of an EEOF even more impractical as the high noise levels make it harder to define common modes of variability across multiple ensemble members. For these two reasons, I decided to instead use a standard EOF rather than an EEOF for the CESM2-LENS output.

3.3.5 Surface Mixed Layer Heat Budget

A heat budget can be used to determine the underlying physical forcings behind changes in ocean temperature tendency (*Stevenson and Niiler*, 1983; *Shearman and Lentz*, 2010). A volume-averaged surface mixed layer heat budget is derived from conservation of heat and conservation of mass equations (*Stevenson and Niiler*, 1983; *Roemmich et al.*, 2005) (see Appendix B for derivation). First, the temperature tendency due to total surface heat flux was calculated as the sum of five individual heat flux components,

$$\frac{Q_{\text{SHF}}}{\rho C_p h} = \frac{Q_{\text{SW}_0} - Q_{\text{SW}_{-h}} + Q_{\text{LW}} + Q_{\text{sen}} + Q_{\text{lat}}}{\rho C_p h} \tag{3.9}$$

where Q_{SHF} is the surface heat flux, Q_{SW_0} is the surface shortwave heat flux, $Q_{\text{SW}_{-h}}$ is the shortwave heat flux at the MLD, Q_{LW} is the longwave heat flux, Q_{sen} is the sensible heat flux, Q_{lat} is the latent heat flux, ρ is the seawater density, C_p is the specific heat capacity of seawater ($\rho C_p = 2.439 \times 10^7 Jm^{-3\circ}C^{-1}$), and h is the MLD.

Using the CESM2-LENS model output, a mixed layer temperature tendency anomaly

heat budget was created with a minimal residual (*Moisan and Niiler*, 1998) (see Appendix B),

$$\underbrace{\frac{\partial \overline{T}}{\partial t}}_{\text{Temperature tendency}} = \underbrace{-\overline{\mathbf{u}} \cdot \nabla_H \overline{T}}_{\text{Horizontal advection}} \underbrace{-\frac{\overline{T} - T_{-h}}{h} w_{-h}}_{\text{Vertical advection}} + \underbrace{\frac{Q_{\text{SHF}}}{\rho C_p h}}_{\text{Air-sea heat flux}} \underbrace{-\frac{1}{h} k_z \frac{\partial T}{\partial z}_{-h}}_{\text{Vertical Mixing}} + \underbrace{\overline{\nabla_H \cdot (k_{\text{h}} \nabla_H T)}}_{\text{Horizontal mixing}} \underbrace{-\frac{\overline{T} - T_{-h}}{h} \left(\frac{\partial h}{\partial t} + \vec{u}_{-h} \cdot \nabla_H h \right)}_{\text{MLD tendency and lateral induction}}, \tag{3.10}$$

where $\overline{T}$ is the surface mixed layer temperature, t is time, $\mathbf{u}$ is horizontal velocity, ∇_H is the horizontal gradient operator, k_z is the vertical diffusivity coefficient, and k_{h} is the horizontal diffusivity coefficient. Each term was vertically averaged over the MLD, shown here by $\bar{\cdot} = \frac{1}{h} \int_{-h}^{0} \cdot \text{dz}$; $\cdot_{-h}$ indicates a variable taken at $-h$.

Horizontal diffusion was determined by finding the sum of eddy-induced advective temperature tendency, Redi temperature tendency, Robert filter temperature tendency, and submeso advective temperature tendency (*Rodgers et al.*, 2021). A residual was determined by subtracting the horizontal advection, vertical advection, air-sea heat flux, and horizontal diffusion from the temperature tendency. The vertical mixing terms from the CESM2-LENS output only accounts for the air-sea heat flux input at the surface. In theory, the heat budget residual represents the vertical mixing not associated with air-sea heat flux. In practice, it also includes model and numerical error.

The volume average of each term (being an average of the already vertically averaged terms) was determined for each of the predefined regions. The detrended anomaly of each heat budget term was determined by subtracting a 1920 to 1950 climatology and removing the linear trend over the entire time series of each term.

3.4 Results

Using EOF results, modes of variability are first isolated. The AMO and NAO indices are then derived for each of the ensemble members. After this, cross-correlations and the power spectral density are determined for the observed AMO and NAO indices, CESM2-derived AMO and NAO indices, and CPC1 and CPC2. After this heat budget averages and ocean/atmospheric variable map averages are calculated over AMO and NAO formation/dissipation years.

3.4.1 CESM2-Defined AMO and NAO

Yearly-averaged AMO and NAO indices were created for each of the ten CESM2-LENS ensemble members (Fig. 3.1). The time series includes the ensemble mean, ± 1 ensemble standard deviation, and the annual observed AMO and NAO indices. The CESM2-derived AMO index (Fig. 3.1, top plot) mean and standard deviation show a clear multidecadal oscillation with positive phases approximately located at 1875-1900, 1920-1950, and 1990-2015. The observed AMO index also shows positive phases at approximately the same time (*Trenberth and Shea*, 2006). The individual ensemble member AMO indices are not always temporally consistent with individual peaks being seen around 1960-1970 and 1970-1985. Negative phases are also consistent between the CESM2-derived and observed AMO indices. Troughs can be seen in both around 1900-1920 and 1960-1990. The spread (standard deviation) of the CESM2-derived AMO indices is temporally consistent staying around $\pm 0.5^{\circ}C$ for the entire time series.

The individual ensemble CESM2-derived NAO indices (Fig. 3.1, bottom plot) show a much higher frequency of variability when compared to the ensemble mean AMO index. This is again mirrored in the observed NAO index (*Hurrell et al.*, 2003). The mean of the CESM2-derived NAO index has a lower amplitude than each of the individual ensemble NAO indices. This suggests that the NAO indices are out of phase across ensemble members. This is the opposite to the individual ensemble members AMO

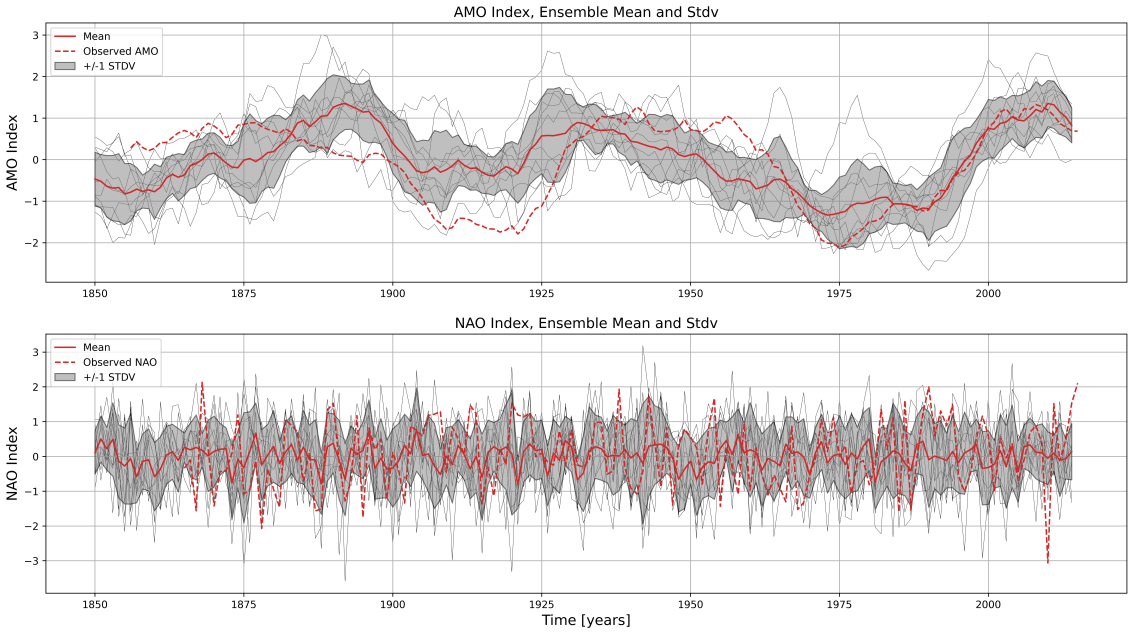

Figure 3.1: Annual CESM2-derived AMO (*top plot*) and NAO (*bottom plot*) indices from 1850 to 2015. The individual ensemble member(*solid grey lines*), the mean index (*solid red line*) and ± 1 ensemble standard deviation (*grey shaded area*) are shown for both the AMO and NAO indices. The annual observed AMO and NAO indices (*dashed red line*) are also shown.

indices where the phases mostly line up. The observed NAO index also shows a yearly-to-multiyear oscillation similar to the NAO indices derived from the CESM2-LENS. Upon first observation, it is difficult to determine similarities between the in-situ and CESM2-derived NAO indices due to the increased frequency of oscillation.

High correlation coefficients were found between the mean CESM2-derived AMO index and the observed AMO index (Appendix C, 0.45 at 0 years lag). There is also a clear wave pattern to the cross-correlation with peaks around -65 years and 65 years lag (Appendix C, 0.67 and 0.34 respectively). This suggests a multidecadal structure in both the CESM2-derived and observed AMO indices, one that can be clearly seen in both of the time series (Fig. 3.1, top plot). Most AMO indices of the individual ensemble members follow the mean. However, there are noticeable differences around the 65 year lag peak.

Consistently low correlation coefficients were found between the CESM2-derived and observed NAO indices (Appendix C, -0.005 at 0 years lag). The mean correlation

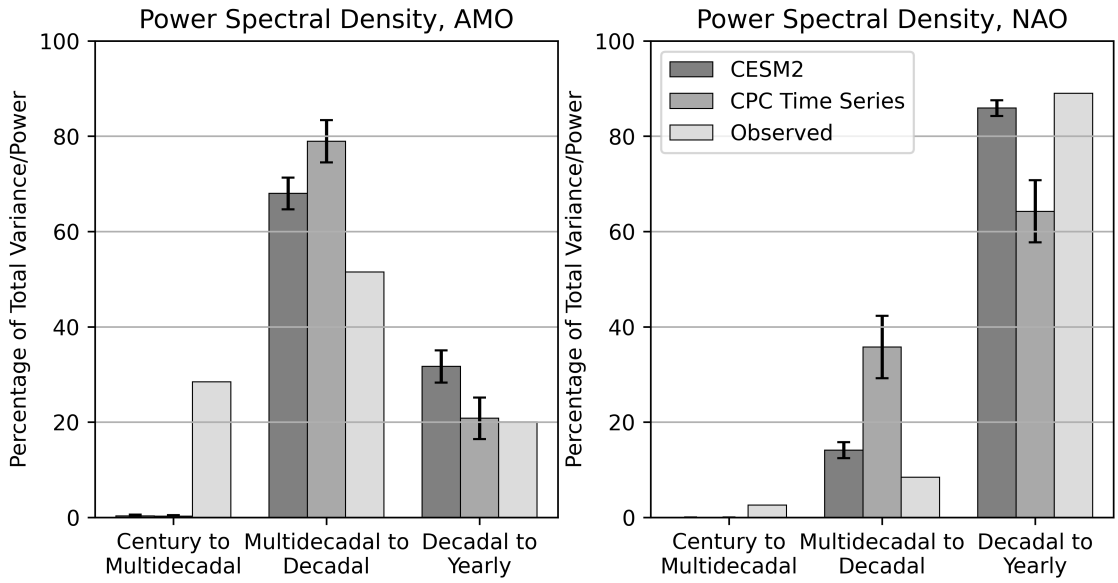

Figure 3.2: Power spectral density plots for the observed, CESM2-derived, and CPC time series AMO (*left column*) and NAO (*right column*) indices. The power spectral density plots were integrated over three defined periods; century to multidecadal, multidecadal to decadal, and decadal to yearly. The mean and standard deviation of the CESM2-derived AMO and NAO indices and CPC time series (*left and middle bars, darker colouring*) is shown along with the power spectral density plot for the observed AMO and NAO index (*right bars, lighter colouring*).

coefficient is also lower than the individual ensemble members indices suggesting that they are out of phase similar to what occured in the CESM2-derived NAO time series (Fig. 3.1, bottom plot).

The power spectral density plots (Fig. 3.2) were integrated over specific frequencies and divided by the total power spectral density sum to determine the percentage of total variance/power that is found in century to multidecadal (100+ to 100 year period), multidecadal to decadal (100 to 10 year period), and decadal to yearly periods (10 to 1 year period).

Most ($68.37\% \pm 3.32\%$) of the CESM2-derived AMO indices total variance is found in periods larger than 10 years (Fig. 3.2, left plot). This is again the result of the strong multidecadal signal seen in the AMO time series (Fig. 3.1, top plot). The vast majority (82.25%) of the observed AMO index variance is within the century to multidecadal and multidecadal to decadal periods. This is expected as both the CESM2-derived and observed AMO indices oscillate with a period of 60-80 years (*Trenberth and Shea*, 2006; *Deser et al.*, 2010). The decadal to yearly percentage of total variance for both CESM2-derived and in-situ AMO indices is relatively low, $31.19\% \pm 3.42\%$ for the CESM2-derived AMO indices and 17.75% for the observed AMO index.

For the CESM2-derived NAO indices, $14.15\% \pm 2.08\%$ of the variance is found within the multidecadal to decadal period rage and $85.85\% \pm 2.08\%$ is found within the decadal to yearly period range (Fig. 3.2, right plot). For the in-situ NAO index, 18.54% is found within the century to multidecadal and multidecadal to decadal period range and 81.46% is found within the decadal to yearly period range. This suggests that although the phasing between the ensemble members NAO indices with the in-situ NAO index is off, both groups contain similar time scales of variability.

3.4.2 Modes of Variability in CESM2-LENS

An EOF was performed on the detrended mixed layer temperature tendency anomaly from each of the ten ensemble members between 1850 and 2015. Using the ensemble member's

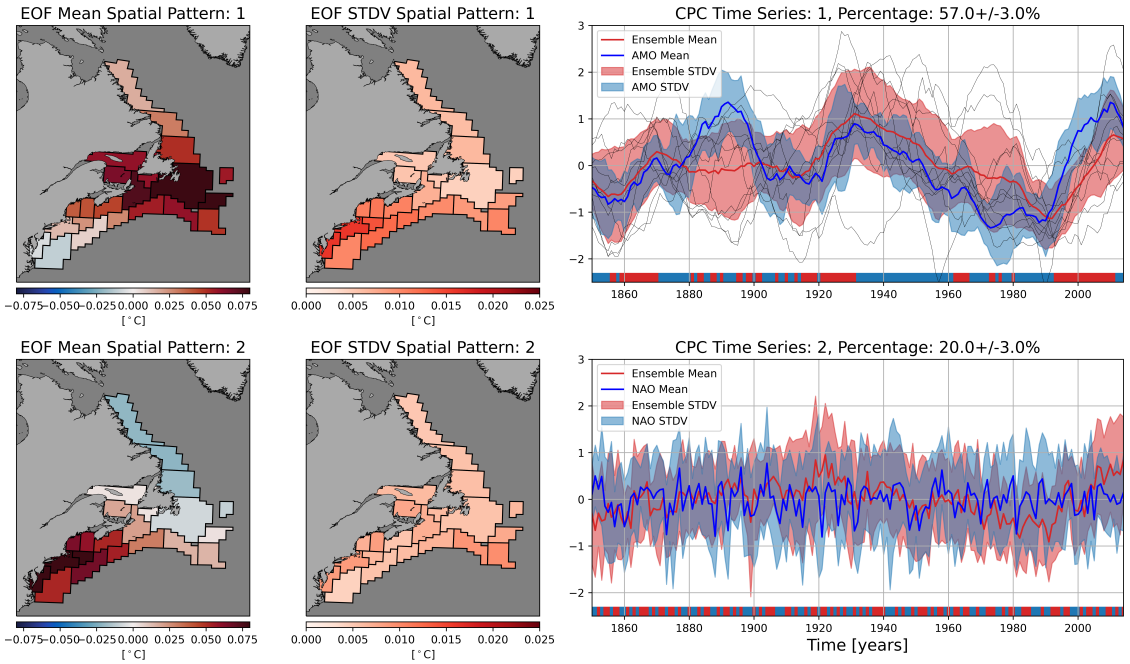

Figure 3.3: EOF spatial pattern mean and standard deviation (*first and second columns respectively*) and CPC time series (*right column*). The EOF and CPC rows correspond to the leading two modes from the yearly detrended mixed layer temperature tendency anomaly between 1850 and 2015. The CPC time series mean (*solid red line*) and standard deviation (*shaded red area*) along with the CESM2-derived AMO and NAO mean (*solid blue line*) and standard deviation (*shaded blue area*) are shown (*right column*). The percentage of explained variability is given above the CPC time series. The first mode also includes each of the individual ensemble members PC time series (*grey lines*). Positive gradient formation years (*red areas*) for the mean CPC1 and CPC2 are shown along the bottom of the time series. Negative dissipation years are also shown (*blue areas*).

resulting EOF eigenvalues, it was found that modes one and two explained $57.0 \pm 3.0\%$ and $20.0 \pm 3.0\%$ respectively; collectively explaining $77\% \pm 6.0\%$.

EOF mean spatial pattern 1 (Fig. 3.3, first row) has a positive sign throughout most of the regions with a positive pole locate east of Newfoundland. The mode decays to the north and south, over the Labrador Sea and Mid-Atlantic Bight, away from the main pole. The standard deviation across EOFs from all ensemble members increases towards the Mid-Atlantic Bight where the mean EOF is smallest. The mean values in the pole structure are always higher than the corresponding standard deviation. The first modes spatial pattern shows resemblance to the first modes correlated with the AMO from *Loder*

and Wang (2015) and *Loder and Wang* (2019).

CPC1 shows a consistent multidecadal variability with positive phases peaking around 1930 and 2005 and a negative phase around 1980. The CESM2-derived AMO index mostly mirrors CPC1 after 1910 and before 1875. Between these years, the AMO index shows a clear increase around 1900 which is not mirrored in the CPC1 time series. The first mode explains $57.0 \pm 3.0\%$ of the total detrended mixed layer temperature tendency anomaly variance. The CPC1 ensemble spread (standard deviation about the mean) has a similar magnitude of ± 0.75 until the beginning of the 1980s when the standard deviation decreases. The CESM2-derived AMO ensemble spread is consistently less than the spread for the CPC1, at around ± 0.5 for the entire time series.

EOF mean spatial pattern 2 (Fig. 3.3, second row) has a dipolar structure with a positive pole in the Mid-Atlantic Bight and a slight negative pole in the Labrador Sea. The standard deviation of the spatial pattern shows consistently lower values than the mean throughout all regions. This is similar to the second mode correlated with the NAO from *Loder and Wang* (2015) and *Loder and Wang* (2019).

CPC2 shows higher frequency variability throughout the time series superimposed onto a multidecadal oscillation. A clear multidecadal peak can be seen around 1920-1930 and 2000-2015 and a trough around 1850-1860 and 1970-1980. The CESM2-derived NAO index also shows high frequency variability but does not exhibit a multidecadal signal like in the CPC2. The second mode explains $20.0 \pm 3.0\%$ of the total detrended mixed layer temperature tendency anomaly variance. Both the CESM2-derived NAO indices and CPC2 have a much higher spread (standard deviation) than the reported mean indicating that the ensemble members time series are out of phase with one another.

The CESM2-derived AMO and NAO indices were cross-correlated with the two leading PC time series from the EOF results (Appendix C). Each of the PC time series were compared with their corresponding ensemble members AMO or NAO index. Peak correlation values can be seen in both the AMO (Fig. C.1, 0.29) and NAO (Fig. C.1, 0.18)

cross-correlations at lag 0. The AMO cross-correlation retains some of the wave-like structure seen from before (Fig. 3.2, top plot) The NAO cross-correlation outside of of 0 lag remains noisy compared to the AMO cross-correlation results.

The first CPC time series' power spectral density, indicates that $79.12\% \pm 4.35\%$ of the variance is within the multidecadal to decadal period window and $20.80\% \pm 4.35\%$ is within the decadal to yearly period window (Fig. 3.2, left plot). This is similar to the power spectral densities of the CESM2-derived and observed AMO indices and establishes that all three index groups feature prominent multidecadal oscillation. The second CPC time series' power spectral density indicates that $35.76\% \pm 6.53\%$ of the variance is within the multidecadal to decadal period window and $64.24\% \pm 6.53\%$ is within the decadal to yearly period window (Fig. 3.2, right plot). Therefore, both the CPC-derived NAO and CESM2-derived NAO have a similar power spectral density to the observed NAO index.

Results from the cross-correlations, power spectral density plots, and EOF indicate that both the CESM2-derived AMO and NAO indices and CPC time series are accurate representations of the observed AMO and NAO indices and their associated SSTA spatial patterns (*Hurrell et al.*, 2003; *Trenberth and Shea*, 2006; *Deser et al.*, 2010; *Loder and Wang*, 2015, 2019). We assume that because of the accurate representation of the observed AMO and NAO in the CESM2-LENS temperature tendency output, that the physical forcing behind these model-generated AMO and NAO indices is also reasonable.

3.4.3 Anomaly Heat Budget

A temperature tendency anomaly heat budget was created for each of the regions from 1850 to 2015. Years were defined as positive (formation) or negative (dissipation) according to the value of the PC times series in section 3.4.2. The average over all positive years or negative years (composite mean) of each of the heat budget terms across all ensemble members was then calculated and removed from the original terms to leave anomalies; we refer to this as "anomaly heat budget". The standard deviation across ensemble members was also calculated.

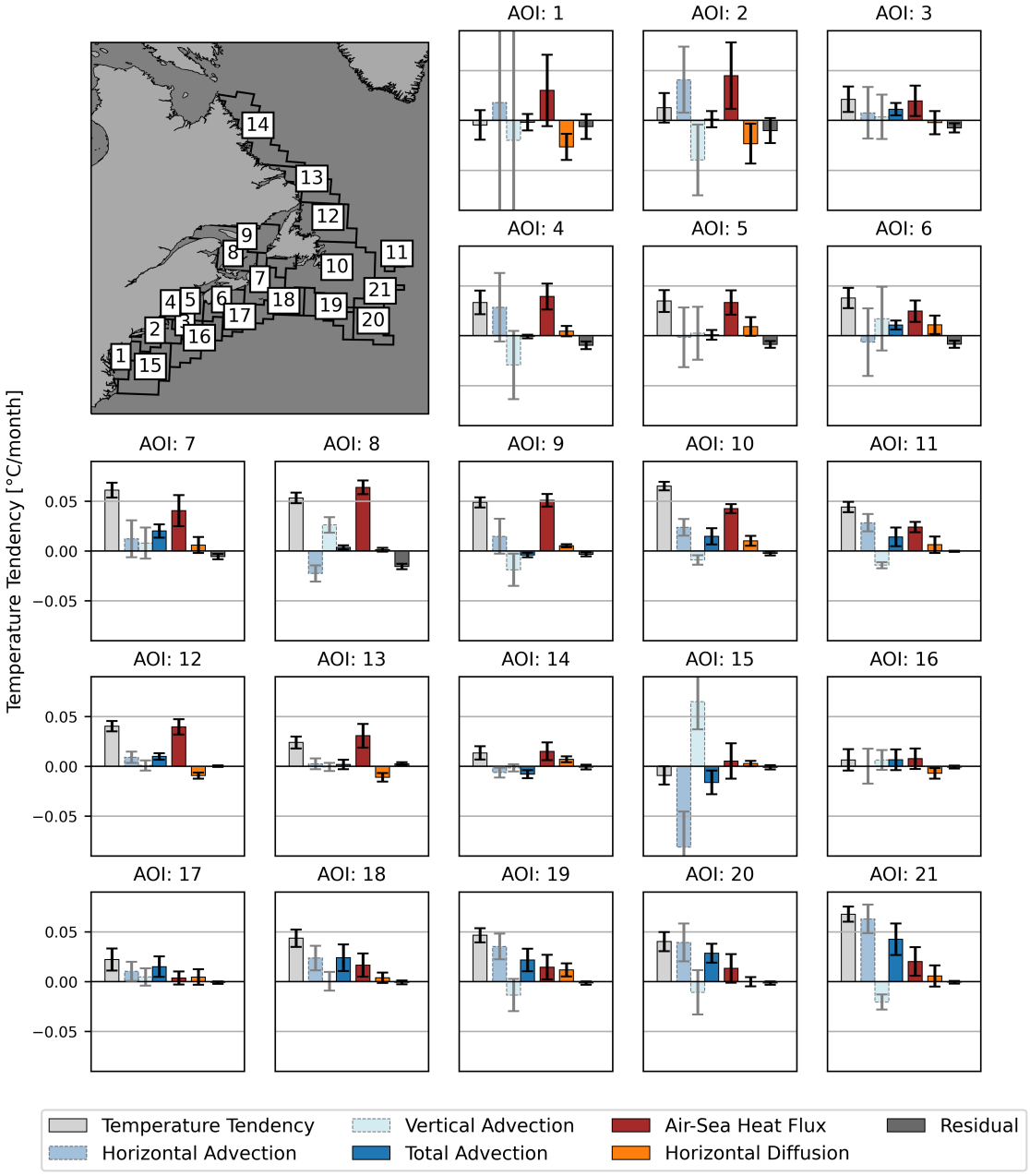

Figure 3.4: Region of interest heat budget terms [$^{\circ}C$/month] averaged over positive PC time series 1 years. Each term has a ± 1 standard deviation uncertainty bar calculated from the ensemble means standard deviation. The horizontal and vertical components of the total advection term (*dark blue*) are shown to left (*dotted outlines, lighter colouring*). The sum of all darker coloured bars equals the temperature tendency (*light grey*) plus the residual (*dark grey*). A reference map is given in the top left corner with each of the regions labelled.

3.4.3.1 First Mode Heat Budget

The composite mean temperature tendency for positive PC1 (Fig. 3.4, light grey bar) follows a similar pattern to the results from the EOF first spatial pattern. Temperature tendency increases towards the location of the positive pole east of Newfoundland (region 10). This increase in temperature tendency is seen in both the shelf regions (7,8,9,10,11,12) and slope regions (18,19,20,21). The standard deviation of the temperature tendency across ensemble members in these regions remains relatively small compared to the mean. The mean AMO formation temperature tendency accurately recreate the AMO SSTA spatial pattern (Fig. 3.3, first row). Throughout most of the regions, the residual temperature tendency (dark grey bar) remains small relative to most of the other heat budget terms.

The total advection (Fig. 3.4, dark blue bar) varies in its contribution to the total temperature tendency depending on region. In the shelf regions (1-14), the total temperature tendency mostly plays a minimal role in the positive total temperature tendency. This is especially the case in regions 1-6, 8, and 9. In some regions, the horizontal advection temperature tendency is equal and opposite to the vertical advection temperature tendency (region 1,2,15). This implies a compensation such that heat advected into the region, either horizontally or vertically, is immediately advected out in the other direction. In regions 7, 10, and 11, the total advection temperature tendency helps to contribute to the positive total temperature tendency but is not the main contributor to the positive mean. In contrast, the slope regions (15-21) total temperature advection is mostly the main contributor to positive total temperature tendency where a strong positive signal can be found (region 17-21).

The air-sea heat flux (Fig. 3.4, dark red bar) also varies depending on whether the region is located on the slope or shelf. In most of the shelf regions with positive total temperature tendencies, the air-sea heat flux is the main contributor to the positive signal. This is apparent in regions 7-10. In the slope regions that show a strong positive signal (region 17-21), the air-sea heat flux contributes roughly the same or less than the positive signal seen in the total advection.

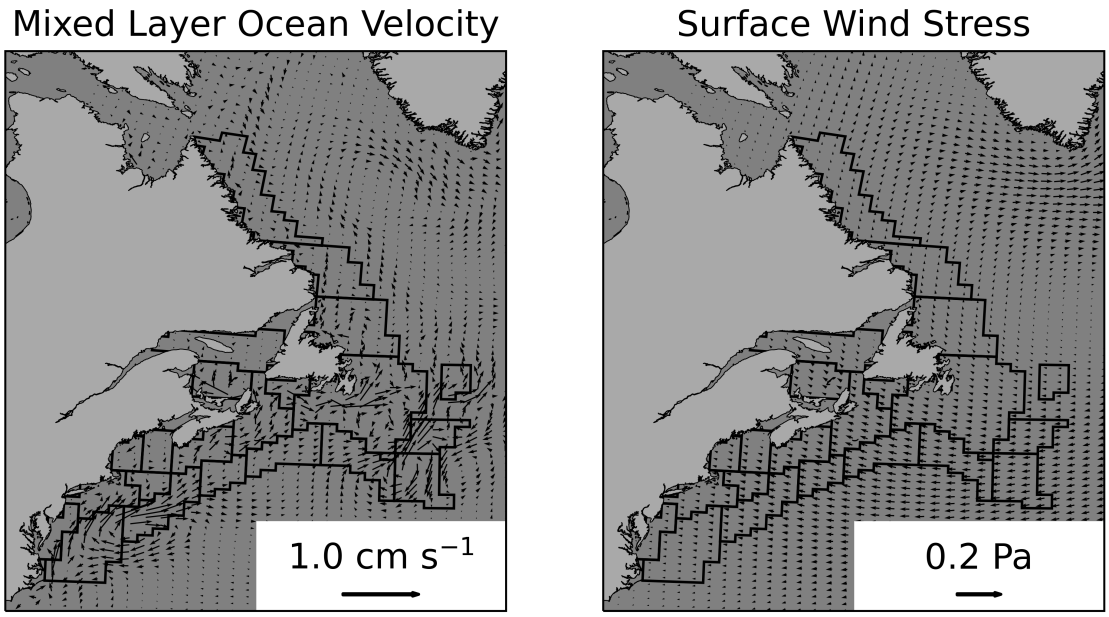

Figure 3.5: Mixed layer ocean current and wind velocity anomalies averaged over positive PC time series years from the first mode. Detrended mixed layer ocean velocity anomaly (*left plot*) and detrended surface wind stress anomaly (*right plot*) are shown here with a quiver key in the bottom right corner of each plot.

Outside of regions 1 and 2, the horizontal diffusion temperature tendency accounts for a minimal amount of the positive temperature tendency anomaly signal. Within regions 1 and 2, the horizontal diffusion term also has a large standard deviation.

3.4.3.2 First Mode Composite Means

Ensemble means of candidate forcing variables were averaged over the first mode's positive years (Fig. 3.5, 3.6). Variables were selected that either directly or indirectly appear in the heat budget equation. For each variable, anomalies were determined and then detrended. All variables, except mixed layer ocean velocity anomaly and surface wind stress anomaly, were spatially averaged into the regions of interest. Regions with air-sea heat flux component standard deviations larger than the mean are represented with a dashed region outline.

During positive PC1 years, the mixed layer ocean velocity anomaly along the slope is not spatially consistent. Two large anomalous gyres can be seen in the slope regions

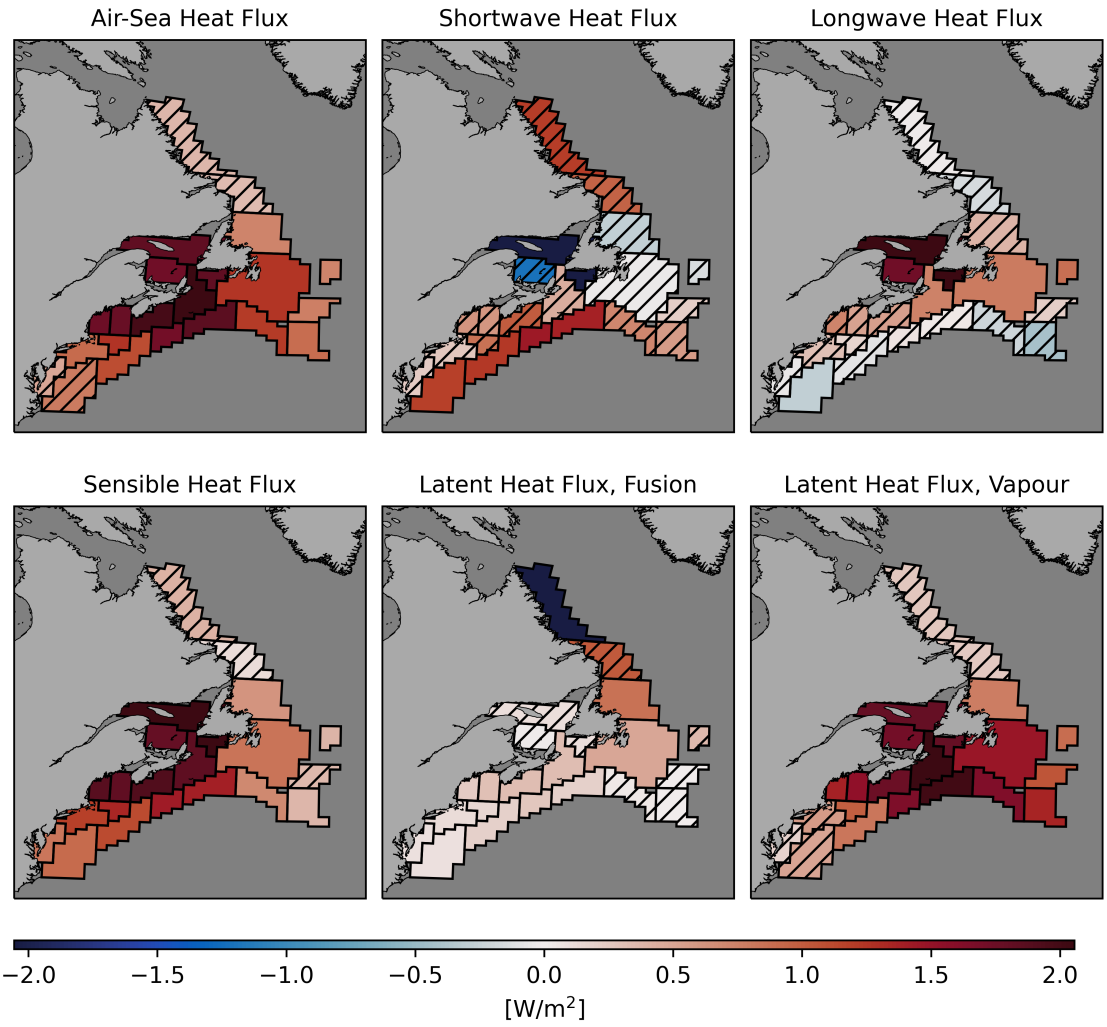

Figure 3.6: Air-sea heat flux terms averaged over positive PC time series years from the first mode. Total air-sea heat flux (*top left plot*), shortwave heat flux (*top middle plot*), surface longwave heat flux (*top right plot*), sensible heat flux (*bottom left plot*), latent heat flux from fusion (*bottom middle plot*), and latent heat flux from vaporization (*bottom right plot*) anomalies were found and then detrended. Areas where the standard deviation is larger than the absolute ensemble mean were marked as insignificant (*dashed regions*).

off the Mid-Atlantic Bight (region 15, 16) and to the southeast of Newfoundland (region 10, 19-21). The magnitude of the mixed layer ocean velocity anomaly in the northeast direction in the southern slope and shelf is the result of these two gyres. Regions 17 and 18 between the two anomalous gyres has a relatively smaller anomaly. The two furthest east slope regions (20, 21) show the mixed layer ocean velocity anomaly travelling in the opposite direction to most of the regions located on the slope. The southern shelf regions (1-11) show no clear structure. The northern shelf regions (12-14) show a slight increase in northward flow. This is all consistent with a reduction in the Labrador Current over our whole region.

The surface wind stress anomaly shows a clear structure throughout all regions. In the southeast, the surface wind stress anomaly is directed west. In the northwest, it is directed north. This implies a larger clockwise rotation and is linked to an atmospheric high pressure cell located in the Labrador Sea.

The total air-sea heat flux, sensible heat flux, and latent heat flux of vaporization all show a similar significant positive polar structure to what is seen in the total temperature tendency (Fig. 3.6). Along the shelf, sensible heat flux and latent heat flux of vaporization both contribute roughly the same amount to the total positive signal (regions 4-9). In the Grand Banks and Flemish Cap, latent heat flux of vaporization has a higher positive anomaly than sensible heat flux (regions 10, 11). In the eastern slope regions, latent heat flux of vaporization consistently shows higher postive anomalies when compared to sensible heat flux (regions 17-21). Shortwave heat flux anomalies are insignificant outside of the western slope regions (15-18) and the northern Gulf of St. Lawrence (region 9).

3.4.3.3 Second Mode Heat Budget

The same averaging over positive years of heat budget terms was done for the second mode PC time series (Fig. 3.7). For the second mode, positive and negative years correspond to NAO formation and dissipation years respectively.

The composite mean heat budget for positive PC2 years (Fig. 3.7) is consistent with the

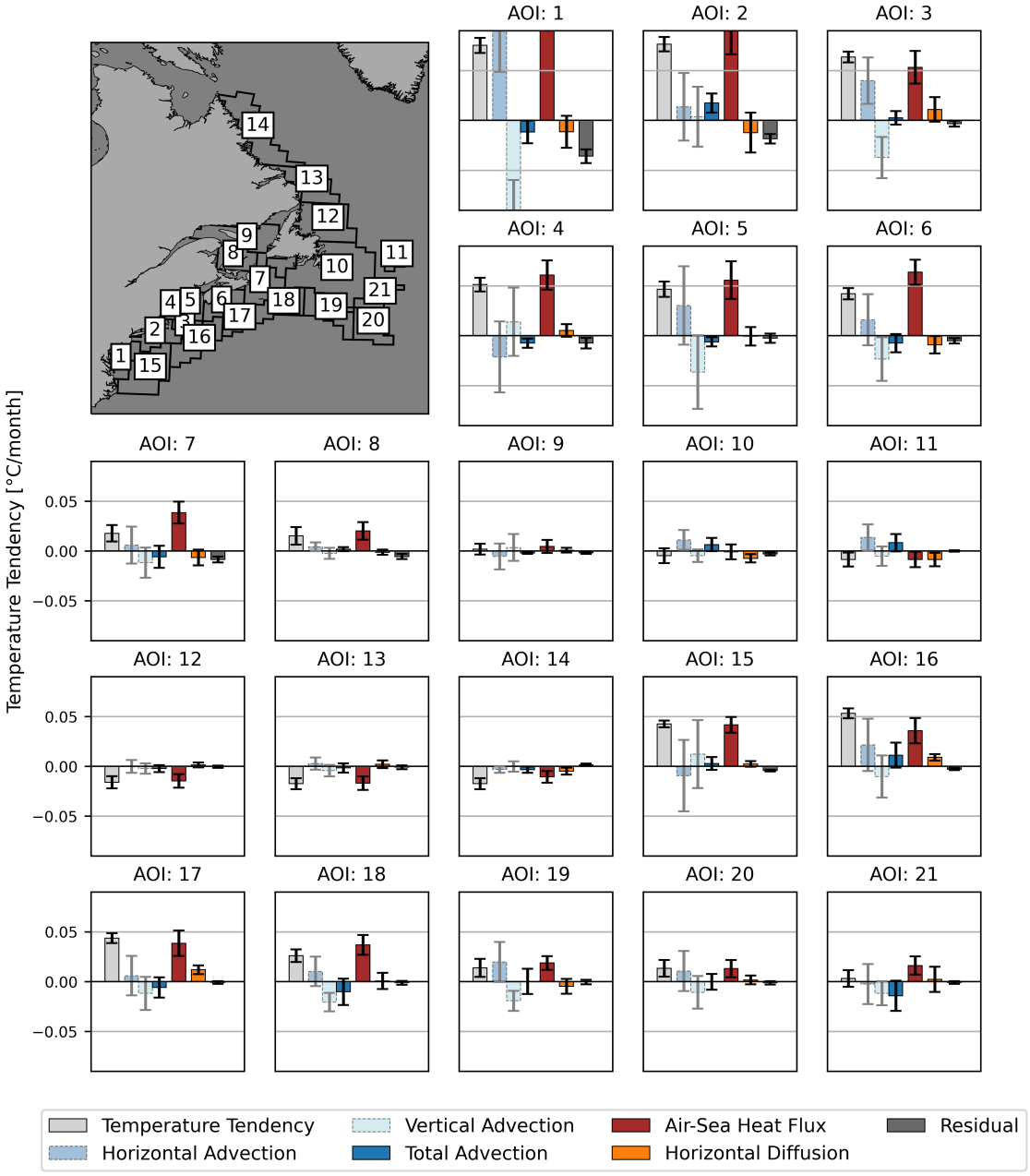

Figure 3.7: Region of interest heat budget terms [$^{\circ}C/$month] averaged over positive PC2 years. Each term has a ± 1 standard deviation uncertainty bar calculated from the ensemble means standard deviation. The horizontal and vertical components of the total advection term (*dark blue*) are shown to left (*dotted outlines, lighter colouring*). The sum of all darker coloured bars equals the temperature tendency (*light grey*) plus the residual (*dark grey*). A reference map is given in the top left corner with each of the regions labelled.

spatial pattern seen in the second mode EOF spatial pattern (Fig. 3.3, second row). The positive pole is located around the Mid-Atlantic Bight (regions 1-3) and a weaker negative pole is located along the Labrador Shelf (regions 12-14). The temperature tendency anomaly during NAO formation years recreate the NAO SSTA spatial pattern (Fig. 3.3). In both poles, the main contributor to the temperature tendency is the air-sea heat flux.

The total advection in both the positive and negative poles is relatively small for most regions. In many of the regions the horizontal advection balances out the vertical advection term (regions 1-6,15,16). Horizontal diffusion also contributes very little to the temperature tendency term in both the poles.

Air-sea heat flux is the main contributor to the dipolar structure in both the shelf and slope regions. The residual is low across all regions except 1 and 2 but still remains lower than the relative temperature tendency and air-sea heat flux terms.

3.4.3.4 Composite Means Second Mode

The mixed layer ocean velocity anomalies during positive PC time series 2 years show an overall weakening of the Gulf Stream and Labrador Current (Fig. 3.8). The Gulf Streams weakening mainly occurs along the slope regions except for in region 2 where the anomalous mixed layer ocean velocity goes in the opposite direction. In many of the shelf regions, the mixed layer ocean velocity anomaly is close to zero, especially in the regions located in the middle of the previously mentioned dipolar structure (regions 7-11).

The surface wind stress anomalies during positive years shows an overall clockwise rotation from which I can associate a high pressure cell (Fig. 3.8). The regions located in the middle of the dipolar structure (regions 7-11,19-21) have a close to zero surface wind stress anomaly.

The total air-sea heat flux, longwave heat flux, sensible heat flux, and latent heat flux of vaporization all have an anomalous dipolar structure with a negative pole in the southern regions and a lesser positive pole in the northern regions (Fig. 3.9). The shortwave and latent heat flux of fusion were found be insignificant for most regions. The northern pole is

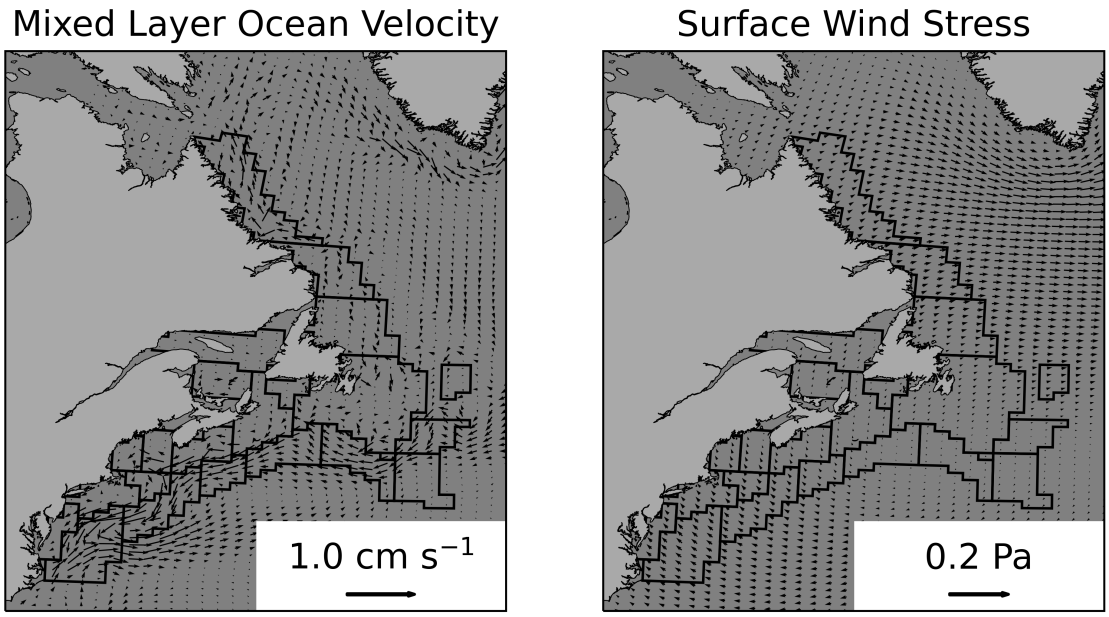

Figure 3.8: Mixed layer ocean current and wind velocity anomalies averaged over positive PC time series years from the second mode. Detrended mixed layer ocean velocity anomaly (*left plot*) and detrended surface wind stress anomaly (*right plot*) are shown here with a quiver key in the bottom right corner of each plot.

mainly made up of the longwave heat flux and sensible heat flux anomalies. The southern pole can be mainly attributed to sensible heat flux and latent heat flux of vaporization anomalies.

3.5 Discussion

This study has demonstrated the dominant physical processes underlying multidecadal temperature variability over the continental shelf and slope in the Northwest Atlantic. Using cross-correlations, power spectral density plots, and EOF analyses, I have established that the CESM2-derived AMO and NAO indices accurately recreate the spatial and temporal patterns associated with the observed AMO and NAO. This has given me the confidence to create a multiple ensemble member mixed layer temperature tendency anomaly heat budget for the predefined regions using the CESM2-LENS output. Evidence was found to support the previously proposed mechanism for the formation of positive AMO events.

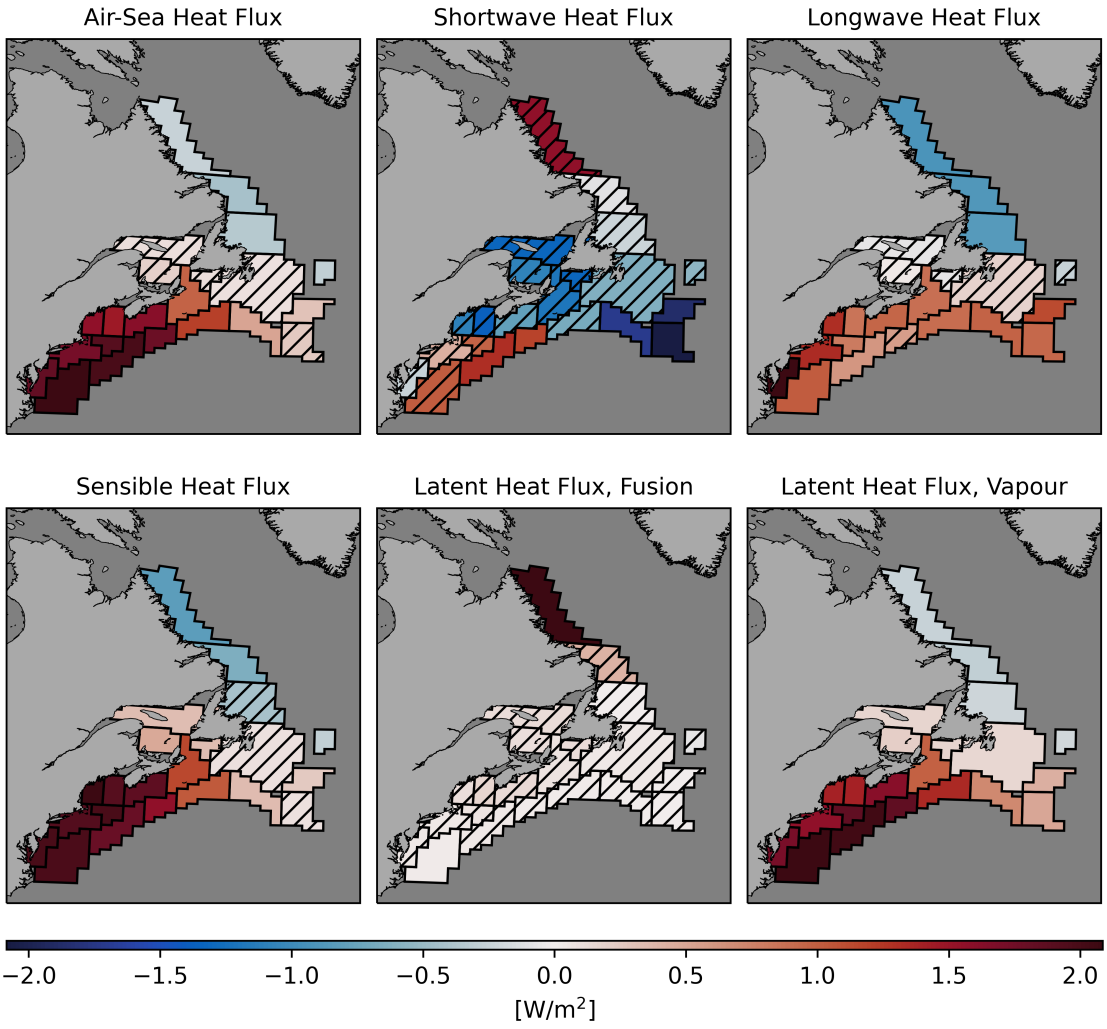

Figure 3.9: Air-sea heat flux terms averaged over positive PC time series years from the second mode. Total air-sea heat flux (*top left plot*), shortwave heat flux (*top middle plot*), surface longwave heat flux (*top right plot*), sensible heat flux (*bottom left plot*), latent heat flux from fusion (*bottom middle plot*), and latent heat flux from vaporization (*bottom right plot*) anomalies were found and then detrended. Areas where the standard deviation is larger than the absolute ensemble mean were marked as insignificant (*dashed regions*).

Evidence was also found that the physical forcing responsible for positive CESM2-derived NAO years matches the current understanding of positive observed NAO years. Lastly, differences were observed in the physical forcing behind AMO formation years between shelf and slope regions that suggest the physical forcing behind the AMO signal differs between the Northwest Atlantic shelf and slope.

Historically, heat budgets have been limited in their spatio-temporal extent due to the lack of available data (*Stevenson and Niiler*, 1983; *Roemmich et al.*, 2005; *Rodgers et al.*, 2021). Using the CESM2-LENS output, a mixed layer temperature tendency anomaly heat budget was calculated for predefined regions from the Mid-Atlantic Bight to the Labrador Shelf (*Rodgers et al.*, 2021). This allowed for the study of yearly-to-multidecadal SSTA variability, specifically AMO and NAO, over multiple AMO cycles. With access to multiple ensemble members, ensemble uncertainty calculations were included for each of the heat budget terms. Again, it is important to note discrepancies between observations and CESM2-LENS output, mainly the incorrect path and separation of the Gulf Stream and the unrealistic sea ice coverage over the Labrador Sea (*Danabasoglu et al.*, 2020). Both of these error could have an effect on multidecadal SSTA variability in the Northwest Atlantic.

AMO formation years occur after positive NAO years and lead to negative air-sea heat flux anomalies in the Labrador Sea (*Wills et al.*, 2019). This drives warm water advection northwards through Atlantic Meridional Overturning Circulation and eventually leads to a positive SSTA in subpolar waters. This is supported by Labrador Shelf heat budget results, which show negative air-sea heat flux anomalies during NAO formation years (Fig. 3.7) and positive temperature tendency through horizontal advection along the slope regions during AMO formation years (Fig. 3.4).

Negative air-sea heat flux anomalies during positive NAO years are driven by anomalously strong westerlies over the subpolar Atlantic (*Wills et al.*, 2019). This is also supported as enhanced westerly winds can be seen over the Labrador Shelf during NAO

formation years (Fig. 3.8). The increased transport of warm waters northwards eventually leads to the formation of a low pressure cell in the Northwest Atlantic subpolar gyre during the peak years of the positive AMO event (*Wills et al.*, 2019). The opposite was found from the surface wind stress anomalies, with a high pressure cell being present over the Northwest Atlantic subpolar gyre (Fig. 3.5). This is possibly due to the surface wind stress anomaly being averaged over all AMO formation years and not peak AMO positive years. During the formation of this low pressure cell, the positive AMO event has reached its maximum.

The increased advection of warm water northwards eventually leads to increased stratification in the Labrador Sea and a slowing down of the Atlantic Meridional Overturning Circulation (*Deser et al.*, 2010; *Wills et al.*, 2019). This will cause the decay of the positive AMO event. The slowing down of warm water transport northwards is seen in the negative horizontal advection during AMO dissipation years (see appendix, Fig. D.1).

The proposed physical forcing behind positive AMO years in the North Atlantic subpolar gyre extends onto the Northwest Atlantic slope but not onto the shelf (*Deser et al.*, 2010; *Wills et al.*, 2019). Throughout the North Atlantic subpolar gyre, increased warm water advection occurs through an enhanced Atlantic Meridional Overturning Circulation (*Deser et al.*, 2010; *Wills et al.*, 2019). This warming is reinforced after the formation of a low pressure cell which drives relatively warm air northwards and leads to positive air-sea heat flux anomalies. Warm temperature tendency anomalies driven by increased horizontal advection are isolated to slope regions, leading to a difference between shelf and slope warming during AMO formation years. Increased temperature tendency due to horizontal advection along the slope leads to a smaller difference between SST and surface air temperature when compared to shelf regions. This leads to a smaller sensible and latent heat flux into the slope regions (*Stevenson and Niiler*, 1983). This is supported by the heat budget results, which show the slope air-sea heat flux anomalies being partly attributed to significant shortwave heat flux (Fig. 3.6). Comparable insignificant shortwave heat flux

occurs in shelf regions but the air-sea heat flux term is still much higher implying a greater contribution of sensible heat flux and latent heat flux of vaporization (Fig. 3.4, 3.6).

Positive NAO years occur when there is a strengthening of the low and high pressure cells centred around Iceland and the Azores respectively (*Deser et al.*, 2010; *Loder and Wang*, 2015, 2019). The ocean loses heat in the subpolar and tropical North Atlantic from the strengthened westerlies and gains heat in the mid-latitudes as the result of diminished wind speeds, mainly through sensible and latent heat flux anomalies (*Deser et al.*, 2010). Anomalous westerlies and diminished wind speeds occurred along the Labrador Shelf and the middle regions respectively during NAO formation years (Fig. 3.8). A dipolar air-sea heat flux structure was also found during NAO formation years, primarily made up of sensible and latent heat flux vapour (Fig. 3.9).

Anomalous Ekman Currents resulting from enhanced northern westerlies and trade winds, cause an enhanced Labrador Current and Gulf Stream, further strengthening the dipolar mixed layer temperature tendency anomaly structure (*Deser et al.*, 2010). For most regions, horizontal advection plays a minor role in the dipolar structure during NAO formation years (Fig. 3.7). Average surface ocean velocity anomalies also fail to show an enhanced Labrador Current and Gulf Stream during NAO formation years (Fig. 3.8).

The use of the CESM2-LENS output has allowed for the creation of a 165-year long mixed layer temperature tendency anomaly heat budget for the Northwest Atlantic slope and shelf regions (*Rodgers et al.*, 2021). The heat budget results, along with ocean/atmospheric variable map averages over AMO/NAO formation and dissipation years have provided further evidence to the proposed mechanism behind positive AMO events. It was also confirmed that the CESM2-LENS output matches observed NAO physical forcing, with the mixed layer temperature tendency anomaly being mostly attributed to anomalous air-sea heat flux. The heat budget was created using multiple CESM2-LENS ensemble members, allowing for ensemble uncertainty calculations in the heat budget results.

Special care was taken to ensure that the model SSTA variability matched observations. This was done using cross-correlations, power spectral density plots, and EOF results. Despite this, further research should be conducted comparing observed ocean/atmospheric variables to the CESM2-LENS model output to ensure accuracy. The CESM2-LENS output also includes a future projection output from 2015 to 2100. I recommend extending the mixed layer temperature tendency anomaly heat budget over the entire covered time period. From this, we could analyze how long-term ocean temperature increase may affect the AMO and NAO indices and their associated SSTA spatial patterns. Using the heat budget, we could also begin to understand the physical forcing behind any potential changes to the AMO and NAO over the next 85 years.

CHAPTER 4

GENERAL DISCUSSION

The aim of this thesis was to analyze the long-term trends and yearly-to-multidecadal variability in SSTA along the Northwest Atlantic shelf and slope, including physical processes and uncertainty. In Chapter 2, the emergence of the anthropogenically-caused climate change signal from natural SSTA variability (time of emergence) was found to occur before 2100 in every predefined region. Significant modes of SSTA variability along the Northwest Atlantic shelf and slope were isolated and linked to the AMO and NAO climate modes. By comparing the resulting AMO and NAO indices with ocean/atmospheric variables known to have an effect on SST, further evidence was found to support how positive NAO years lead to the eventual formation of a positive AMO event (*Wills et al.*, 2019). In Chapter 3, after establishing that the CESM2-LENS output accurately reproduces Northwest Atlantic SST variability, the surface mixed layer heat budget was calculated for each of the predefined regions. Heat budget results show that the formation and dissipation of positive AMO years is driven by air-sea heat flux anomalies in slope regions and by a combination of horizontal advection and air-sea heat flux anomalies in shelf regions. The resulting heat budget terms provided further evidence that positive NAO years increase warm water flow northwards eventually causing the formation of positive AMO years (*Wills et al.*, 2019). Heat budget results also showed that the formation and dissipation of positive NAO years is mainly driven by anomalous air-sea heat flux. This matches the current understanding of the NAO physical forcing (*Deser et al.*, 2010).

An emphasis was put on determining uncertainty in calculations throughout this thesis through the use of multiple data products and ensemble members. Differences across SST data products have been well noted in the past and so it was deemed important to include some estimate of error if possible (*Loder and Wang*, 2015, 2019; *Kent et al.*, 2021). In Chapter 2, five different global SST data products were used and the subsequent analysis considered them all jointly, as representing spread about the unknown true SST. An EEOF was used, allowing all data products to be considered together, rather than the standard EOF in order to consider cross-data product variability when defining Northwest Atlantic modes of variability. In Chapter 3, multiple ensemble members were used from the CESM2-LENS so that the uncertainty of heat budget results could be determined in regards to model ouput variability.

A heat budget can be used to determine the dominant physical forcings behind variability in ocean temperature (*Stevenson and Niiler*, 1983; *Roemmich et al.*, 2005). The novel use of the CESM2-LENS output allowed for the creation of a heat budget over a 165-year time period covering the entire Northwest Atlantic shelf and slope from the Mid-Atlantic Bight to the Labrador Shelf. Historically, heat budgets results have been spatially and temporally limited due to the lack of available data (*Stevenson and Niiler*, 1983; *Roemmich et al.*, 2005). This limits the ability to study AMO given its 60-70 year period and large area of influence (*Deser et al.*, 2010; *Loder and Wang*, 2015, 2019).

The CESM2-derived AMO is comprised of a large positive SSTA polar structure centred south of Newfoundland with an accompanying time series that has a period of approximately 60-70 years (Fig. 3.3, first row). The CESM2-derived AMO accurately recreates the spatio-termporal SSTA pattern associated with the observed AMO index (*Deser et al.*, 2010; *Loder and Wang*, 2015, 2019). Along the Northwest Atlantic shelf, the SSTA is mainly driven by anomalous air-sea heat fluxes (Fig. 3.4). In the slope regions, the SSTA is driven by a combination of anomalous horizontal advection and air-sea heat flux. The CESM2-derived NAO SSTA spatial pattern has a dipolar structure with a positive pole in

the southern regions around the Mid-Atlantic Bight and a weaker negative pole to the north along the Labrador Shelf (Fig. 3.3, second row). The accompanying time series contains mostly decadal-to-yearly period variability. The SSTA spatio-temporal pattern associated with the observed NAO is also accurately portrayed in the CESM2-derived NAO. In both the shelf and slope regions, the SSTA is mainly driven by anomalous air-sea heat flux (Fig. 3.7).

One of the main goals of this thesis was to gain a better understanding of the physical forcing behind how the AMO and NAO climate modes are expressed in SSTA along the Northwest Atlantic shelf and slope. In Chapter 3, evidence was found showing that the main physical forcing behind the SSTA spatial pattern associated with the AMO, was air-sea heat flux anomalies in the shelf regions, and a combination of horizontal advection and air-sea heat flux anomalies in the slope regions. Evidence was found in chapters 2 and 3 supporting the current hypothesis explaining the switch from positive NAO years to positive AMO years (*Wills et al.*, 2019). The results of Chapters 2 and 3 further support the current understanding of how the NAO and AMO climate modes interact on multidecadal time scales and how positive NAO years may be an indicator of future positive AMO years (*Wills et al.*, 2019). Both chapters also show that the main physical forcing behind the ocean expression of the NAO is from air-sea heat flux anomalies. This matches the current understanding of NAO physical drivers (*Deser et al.*, 2010).

In chapter 3, heat budget results suggest that the physical forcing behind positive SSTA anomalies differs between the shelf and slope in the Northwest Atlantic. Along the slope the physical forcing matches that seen in middle of the North Atlantic, where positive AMO years are mainly the result of enhanced horizontal advection reinforced by positive air-sea heat flux (*Deser et al.*, 2010; *Wills et al.*, 2019). On the shelf, positive AMO events are mainly attributed to air-sea heat flux only. This was not noted in Chapter 2 as comparisons between physical forcing variables on SSTA could not be done with cross-correlation results. Further research using observation-based datasets should be conducted

to determine if the physical forcing behind the SSTA expression of AMO differs on the Northwest Atlantic shelf versus the slope.

The calculated time of emergence for the Northwest Atlantic slope and shelf regions are representative of a larger anthropogenically-induced global warming signal (*Bindoff et al.*, 2019; *Alexander et al.*, 2020). The time of emergence are all within 70 years of today, possibly a reflection of how the long-term trends in Northwest Atlantic SST are anomalously high when compared to the global mean (*Loder and Wang*, 2015, 2019; *Alexander et al.*, 2020). In combination with existing multidecadal variability, this increase in mean SSTA will most likely increase the number of extreme temperature events in the Northwest Atlantic (*Oliver et al.*, 2018). Marine heatwaves, a type of extreme temperature event, have already increased in frequency and duration globally from 1925 to 2016 (*Oliver et al.*, 2021). This has been mainly attributed to accelerated warming through latent heat flux anomalies (*Oliver et al.*, 2021; *Schlegel et al.*, 2021). Given further predicted warming in the Northwest Atlantic, there will likely be a continued increase in marine heatwave frequency and duration, as well as their corresponding impacts on the environment.

In Chapter 2, SSTA time series for each of the regions were compared with the CESM-LENS natural control run to ensure that CESM-LENS output matched observed SSTA variability. In Chapter 3, cross-correlations, power spectral densities, and EOF analysis were used to determine if the CESM2-LENS SSTA variability accurately reflected observed SSTA variability. This was done to establish confidence in the use of CESM-LENS and CESM2-LENS for determining the physical forcing behind AMO and NAO. The fact that CESM2-LENS accurately reproduces the physical drivers behind AMO and NAO provides further support that the CESM2-LENS is a useful tool for SSTA analysis in the Northwest Atlantic. It is recommended that the full spatio-temporal coverage of the CESM2-LENS output be used in future ocean multidecadal variability research.

From the results of the second and third chapters, we can begin to ask further questions. How would the heat budget change if we were to include the 2015-2100 portion of the

CESM2-LENS output? Do long-term ocean temperature trends affect the AMO and NAO spatio-temporal SSTA patterns (and by extension mixed layer temperature tendency anomaly patterns)? How is anthropogenic climate change expressed as a local physical ocean process? These are important questions as they help us to determine the possible magnitude of future SSTA variability in the Northwest Atlantic.

For future work, I recommend further comparisons between CESM2-LENS output with observed ocean data products. It would be beneficial to determine the heat budget from observation-based data products of the Northwest Atlantic slope and shelf over a shorter time period. From this, we could see if the results are consistent beyond the similarities in SSTA and extend to other ocean/atmosphere variables. When using climate model output, it is recommended that all ensemble members be used so that ensemble variability is included in future results. When possible, an emphasis should be put on considering cross-dataset variability and determining the corresponding uncertainty in any trend and variability calculations. An example of this is the use of an EEOF, which allows for multiple EOF spatial patterns or PC time series.

In Chapter 2, observation-based data products were used blindly, where each data product was one realization of the true unknown SST. Uncertainty in the individual data products was not considered when calculating the mean and standard deviation of the SST. In the future, an assessment of quality could be conducted for each of the data products, to see if the density of observations are spatially or temporally dependent. In Chapters 2 and 3, CESM-LENS and CESM2-LENS were used for time of emergence and heat budget results rather than observation-based data products. It is important to repeat that models do not perfectly recreate observations. Lastly, EOF results were interpreted as AMO and NAO rather than the CESM2-derived AMO and NAO. This allows for differences between the PC time series and AMO and NAO to carry over into the heat budget and composite mean results.

The importance of understanding the physical forcing behind multidecadal oscillation

in the Northwest Atlantic has become more important than ever with increasing ocean temperatures. In this thesis, an initial understanding of how the SSTA spatio-temporal patterns associated with the AMO and NAO climate modes occurs along the Northwest Atlantic shelf and slope is presented. Further research is recommended on how to accurately predict future Northwest Atlantic shelf and slope multidecadal variability as its impact on local communities and wildlife cannot be ignored.

APPENDIX A

EEOF RESULTS AND MULTIPLE SPATIAL PATTERNS

Fig. A.1 shows the five EOF spatial patterns resulting from the EEOF performed on the combined observation-based SSTA dataset. Each of the EOF spatial patterns correspond to one of the individual SSTA datasets. The spatial resolution differs between each dataset but each region of interest contains at least one SSTA gridcell which later on allows us to combine regions of interest. The structure of the spatial patterns for the first three modes is relatively constant across each of the five EOF spatial patterns. The boundaries of the region of interest were taken from the SODA dataset. Spatial patterns differ in the magnitude of the pole, with ERSST showing the largest absolute values for each of the three modes. The PC time series is the same as those shown in Fig. 2.6, without the uncertainty.

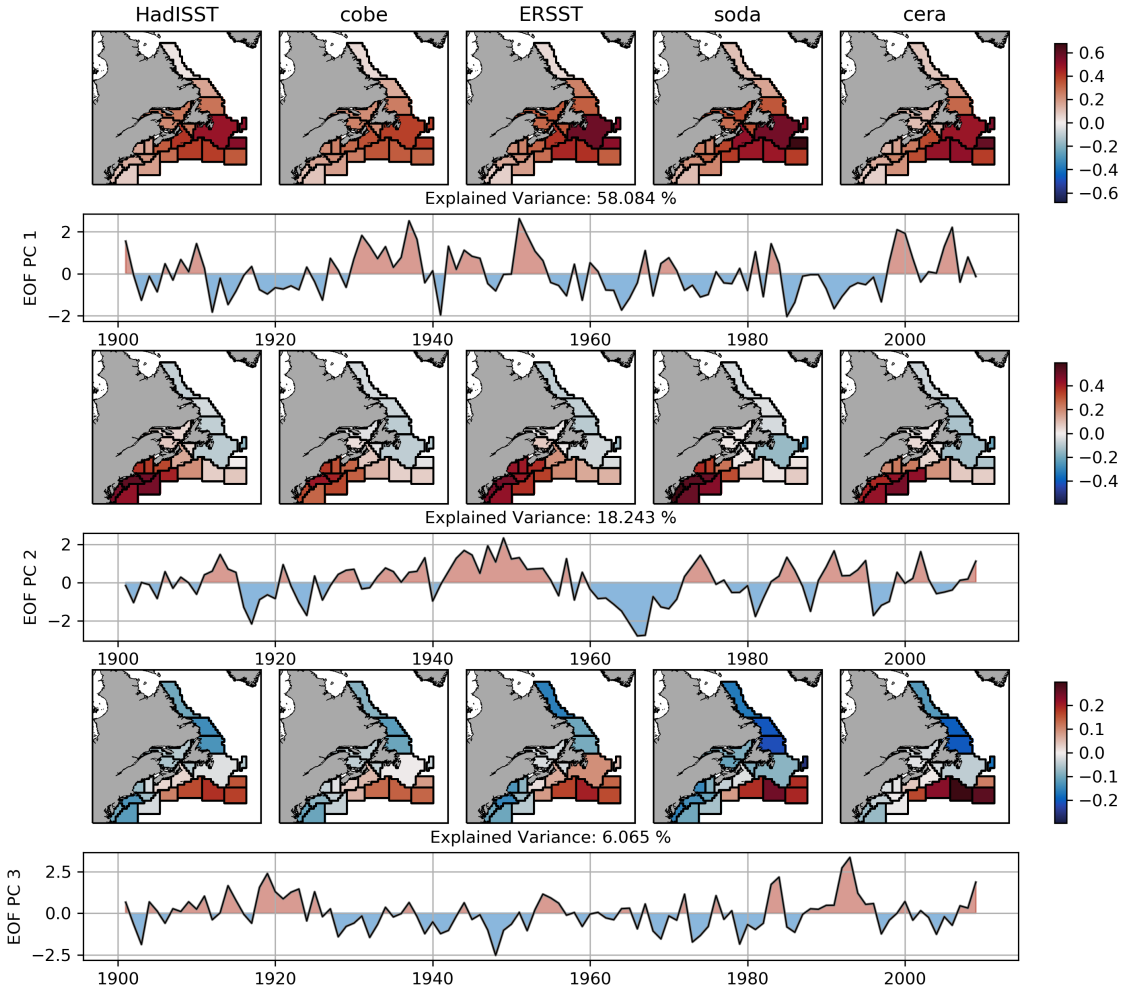

Figure A.1: EEOF results for the first three modes. The five EOF spatial patterns correspond to the five observation-based datasets. The accompanying PC time series and explained variance percentage are given below the EOF spatial patterns.

APPENDIX B

SURFACE MIXED LAYER HEAT BUDGET DERIVATION

Here, we will derive an equation for the tendency of surface mixed layer temperature using a heat budget approach following *Moisan and Niiler* (1998). First, we start with the conservation of mass and conservation of heat equations,

$$\frac{\partial u}{\partial x} + \frac{\partial v}{\partial y} + \frac{\partial w}{\partial z} = 0 \tag{B.1}$$

$$\rho C_p \left(\frac{\partial T}{\partial t} + \nabla \cdot (\vec{v}T) - \nabla_H \cdot k_H \nabla_H T - \frac{\partial}{\partial z} k_z \frac{\partial T}{\partial z} \right) = \frac{\partial q}{\partial z} \tag{B.2}$$

where ρ is the seawater density, C_p is the specific heat of seawater, T is the seawater temperature, $\vec{v}$ is the velocity ($\vec{v} = (u, v, w)$), k_H is the horizontal eddy diffusivity, k_z is the vertical eddy diffusivity, and q is the vertical heat flux, ∇ is the 3D gradient operator $(\frac{\partial}{\partial x}, \frac{\partial}{\partial y}, \frac{\partial}{\partial z})$ and ∇_H is the 2D (horizontal) gradient operator $(\frac{\partial}{\partial x}, \frac{\partial}{\partial y})$. By dividing both sides by ρC_p and expanding the 3D gradient of the velocity multiplied by the temperature, the equation can be rewritten as,

$$\frac{\partial T}{\partial t} + \nabla_H \cdot (\vec{u}T) + \frac{\partial (wT)}{\partial z} - \nabla_H \cdot k_H \nabla_H T - \frac{\partial}{\partial z} k_z \frac{\partial T}{\partial z} = \frac{1}{\rho C_p} \frac{\partial q}{\partial z}, \tag{B.3}$$

where $\vec{u}$ is the horizontal velocity ($\vec{u} = (u, v)$). Each of the terms is now vertically integrated over the surface mixed layer, from $z = -h$ to $z = 0$,

$$\frac{\partial \overline{T}}{\partial t} + \frac{\overline{T} - T_{-h}}{h}\frac{\partial h}{\partial t} + \nabla_H \cdot \overline{\vec{u}T} + \frac{\overline{\vec{u}T} - (\vec{u}T)_{-h}}{h} \cdot \nabla_H h - \frac{(wT)_{-h}}{h} - \overline{\nabla_H \cdot k_H \nabla_H T} + \frac{1}{h} k_z \frac{\partial T}{\partial z}_{-h} = \frac{Q}{\rho C_p h} \tag{B.4}$$

where $\bar{\cdot} = \int_{-h}^{0} \cdot \mathrm{dz}$. The vertical integral of $\frac{\partial q}{\partial z}$ over the mixed layer is equal to Q, the incoming air-sea heat flux (Q_0) (shortwave, longwave, latent, sensible) minus the shortwave heat flux through the bottom layer (Q_{-h}). The first term from B.3 via Leibniz's Integral Rule results in the mixed layer temperature tendency (B.4, first term) plus a MLD tendency term ($\frac{\partial h}{\partial t}$) multiplied by the difference between the average mixed layer temperature and the temperature at the MLD divided by the MLD (h) (B.4, second term). The fourth term is the result of the vertical integral of the second term from equation B.3. The vertical integral of the horizontal advection of temperature over the mixed layer is equal to the average horizontal advection of temperature in the mixed layer (equation B.4, third term) plus the MLD horizontal gradient multiplied by the difference in the horizontal temperature advection divided by the MLD (equation B.4, fourth term). Both the second and fourth term of B.4 arise from $h = h(x, y, t)$.

We then vertically integrate the conservation of mass equation (B.1),

$$\frac{1}{h}\int_{-h}^{0} \nabla \cdot \vec{v} dz = 0 = \frac{\partial \overline{u}}{\partial x} + \frac{\overline{u} - u_{-h}}{h}\frac{\partial h}{\partial x} + \frac{\partial \overline{v}}{\partial y} + \frac{\overline{v} - v_{-h}}{h}\frac{\partial h}{\partial y} - \frac{w_{-h}}{h}, \tag{B.5}$$

where the second and fourth term arise because h varies in (x, y) and the last term arises because we can assume $w(z = 0) = 0$. B.5 can be rewritten as,

$$\nabla_H \cdot \overline{\vec{u}} + \left(\frac{\overline{\vec{u}} - \vec{u}_{-h}}{h} \right) \cdot \nabla_H h = \frac{w_{-h}}{h}. \tag{B.6}$$

The third term in B.4 ($\nabla_H \cdot (\overline{\vec{u}T})$) can be expanded into $\nabla_H \cdot (\overline{\vec{u}}\,\overline{T}) + \nabla_H \cdot (\overline{\vec{u}'T'})$. B.6 can be substituted into the third term of the previously integrated conservation of momentum equation (B.4) after splitting $\nabla_H \cdot (\overline{\vec{u}}\,\overline{T})$ into $\overline{\vec{u}} \cdot \nabla_H \overline{T} + (\nabla_H \cdot \overline{\vec{u}})\overline{T}$ via the product rule for derivatives,

$$\begin{aligned} &\frac{\partial \overline{T}}{\partial t} + \frac{\overline{T} - T_{-h}}{h} \frac{\partial h}{\partial t} + \overline{\vec{u}} \cdot \nabla_H \overline{T} + \nabla_H \cdot \overline{\vec{u}'T'} - \overline{T} \left(\frac{\overline{\vec{u}} - \vec{u}_{-h}}{h} \right) \cdot \nabla_H h + \\ &\frac{w_{-h}}{h} \overline{T} + \frac{\overline{\vec{u}T} - (\vec{u}T)_{-h}}{h} \cdot \nabla_H h - \frac{(wT)_{-h}}{h} - \overline{\nabla_H \cdot k_H \nabla_H T} + \frac{1}{h} k_z \frac{\partial T}{\partial z}_{-h} = \frac{Q}{\rho C_p h}. \end{aligned} \tag{B.7}$$

Temperature T can be expressed as the MLD average temperature $\overline{T}$ plus the remainder T'. By definition, the MLD average of the remainder $\overline{T'} = 0$. The fifth and seventh term can be added together, and simplified to $\left(\frac{\overline{\vec{u}'T'}}{h} + \frac{\overline{T} - T_{-h}}{h} \vec{u}_{-h} \right) \cdot \nabla_H h$. Here, we assume that $\overline{\vec{u}'T'} = 0$, the previous first term ($\frac{\overline{\vec{u}'T'}}{h}$), as well as the fourth term from equation B.7 ($\nabla_H \cdot \overline{\vec{u}'T'}$) go to 0. Terms containing $\frac{\overline{T} - T - h}{h}$ are gathered together into the final equation,

$$\begin{aligned} \frac{\partial \overline{T}}{\partial t} &= -\overline{\vec{u}} \cdot \nabla_H \overline{T} + \overline{\nabla_H \cdot k_H \nabla_H T} - \frac{1}{h} k_z \frac{\partial T}{\partial z}_{-h} \\ &- \left(\frac{\overline{T} - T_{-h}}{h} \right) \left(\frac{\partial h}{\partial t} + \vec{u}_{-h} \cdot \nabla_H h + w_{-h} \right) + \frac{Q}{\rho C_p h} \end{aligned} \tag{B.8}$$

where the terms from left to right represent the temperature tendency (heat storage rate), horizontal advection, horizontal mixing, vertical mixing, entrainment, and air-sea heat flux. The terms inside the entrainment brackets represent the MLD tendency, lateral induction, and vertical advection respectively. This is the final form of the surface mixed layer heat budget used in Chapter 3.

APPENDIX C

CROSS-CORRELATIONS

The cross-correlation between each of the ensemble members first two PC time series and their corresponding CESM2-derived AMO and NAO indices was determined (Fig. C.1). The cross-correlation between the CESM2-derived AMO and NAO indices and the observed AMO and NAO indices was also found.

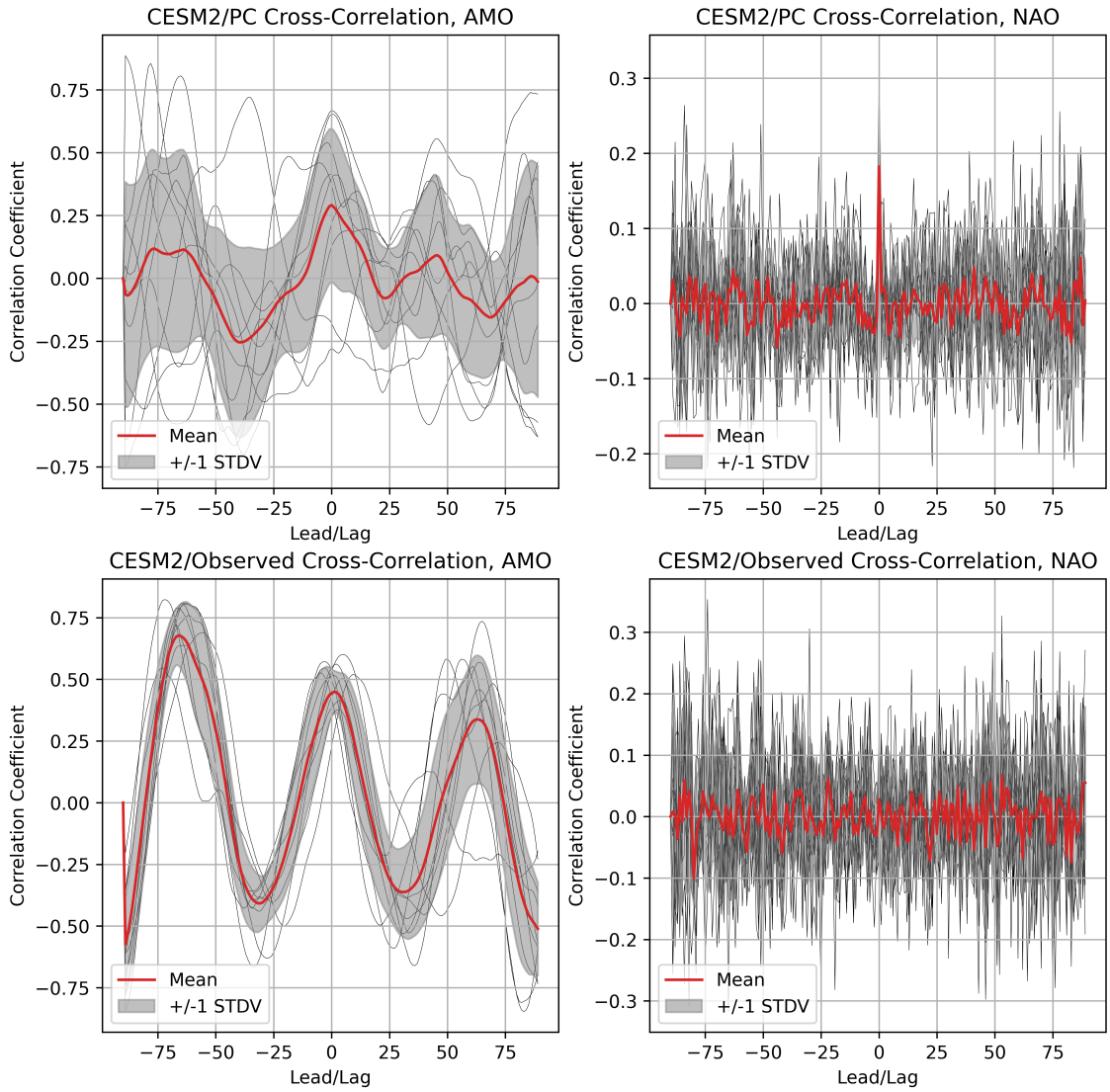

Figure C.1: CPC time series 1 and 2 cross-correlated with their corresponding ensemble members CESM2-derived AMO (*left column*) and NAO (*right column*) index (*top row*). The cross-correlation between the CESM2-derived AMO and NAO indices with the observed AMO and NAO indices is also shown (*bottom row*). The mean cross-correlation (*red line*) is shown along with ± 1 standard deviation (*grey shaded area*). The individual cross-correlations are also shown (*grey lines*).

APPENDIX D

NEGATIVE AMO AND NAO PHASE HEAT BUDGET RESULTS

A heat budget was created for each of the regions from 1850 to 2015 and calculated in terms of detrended mixed layer temperature tendency anomaly rather than in temperature. Using the results from EOFs performed on the CESM2-LENS output, years were defined as positive or negative according to their corresponding ensemble PC times series. Here, I averaged over all negative years, or AMO and NAO dissipation years. The standard deviation of the averages across ensemble members was also determined.

The averages over positive AMO years (Fig. 3.4) are qualitatively the opposite of the heat budget terms found over negative years (Fig. D.1). The same can be said for the positive and negative NAO heat budget terms (Fig. 3.7, D.2). On the shelf, positive AMO years mostly dissipate as the result of negative air-sea heat flux anomalies, while on the slope it is due to both horizontal advection anomalies and air-sea heat flux anomalies. For the second mode corresponding to the NAO, positive NAO years dissipate mostly due to negative air-sea heat flux anomalies throughout the Northwest Atlantic shelf and slope regions.

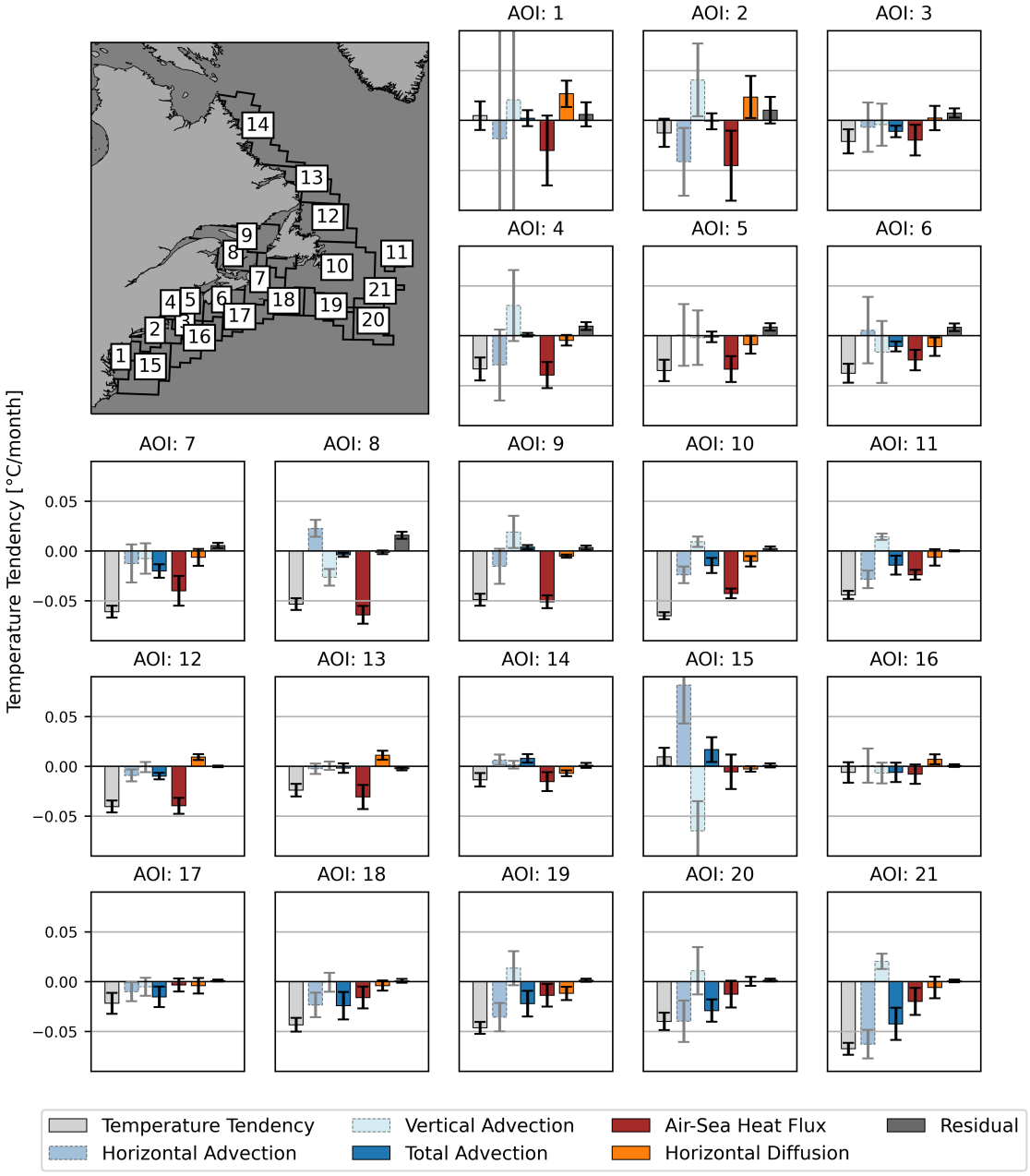

Figure D.1: Region of interest heat budget terms [$^{\circ}C$/month] averaged over negative PC time series 1 years. Each term has a ± 1 standard deviation uncertainty bar calculated from the ensemble means standard deviation. The horizontal and vertical components of the total advection term (*dark blue*) are shown to left (*dotted outlines, lighter colouring*). The sum of all darker coloured bars equals the temperature tendency (*light grey*) plus the residual (*dark grey*). A reference map is given in the top left corner with each of the regions labelled.

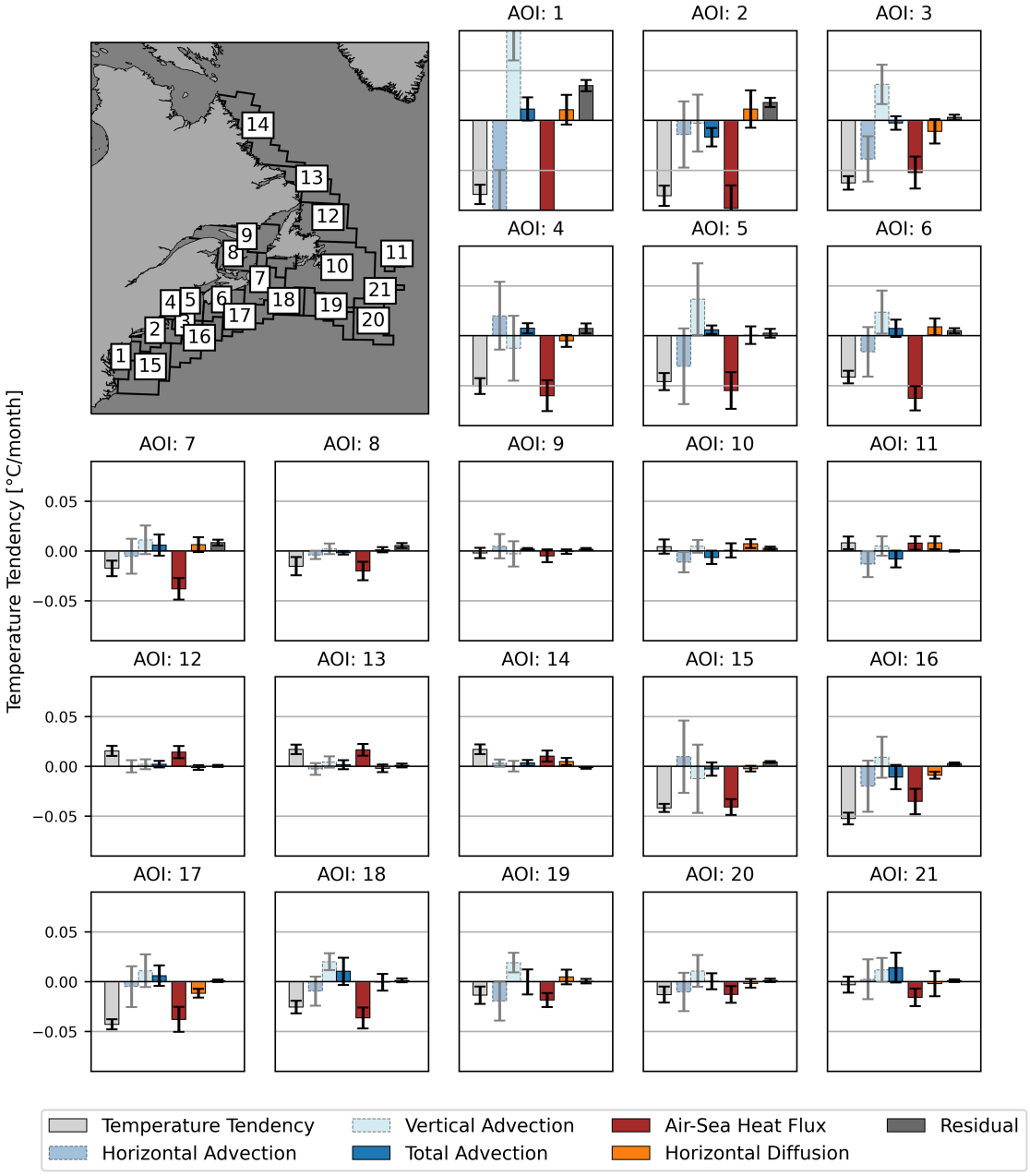

Figure D.2: Region of interest heat budget terms [$^{\circ}C$/month] averaged over negative PC time series 2 years. Each term has a ± 1 standard deviation uncertainty bar calculated from the ensemble means standard deviation. The horizontal and vertical components of the total advection term (*dark blue*) are shown to left (*dotted outlines, lighter colouring*). The sum of all darker coloured bars equals the temperature tendency (*light grey*) plus the residual (*dark grey*). A reference map is given in the top left corner with each of the regions labelled.

BIBLIOGRAPHY

Alexander, M. A., and C. Deser, A Mechanism for the Recurrence of Wintertime Midlatitude SST Anomalies, *Journal of Physical Oceanography*, *25*, 122–136, 1995.

Alexander, M. A., S. I. Shin, J. D. Scott, E. Curchitser, and C. Stock, The response of the Northwest Atlantic Ocean to climate change, *Journal of Climate*, *33*, 405–428, 2020.

Bindoff, N. L., W. W. L. Cheung, J. G. Kairo, J. Aristegui, V. A. Guinder, R. Hallberg, N. Hilmi, N. Jiao, M. S. Karim, L. Levin, S. O'Donoghue, S. R. Purca Cuicapusa, B. Rinkevich, T. Suga, A. Tagliabue, and P. Williamson, IPCC Changing Ocean, Marine Ecosystems, and Dependent Communities, *IPCC Special Report on the Ocean and Cryosphere in a Changing Climate*, pp. 447–588, 2019.

Chen, K., H. Ruoying, B. S. Powell, G. G. Gawarkiewicz, A. M. Moore, and H. Arango, Data Assimilative Modeling Investigation of Gulf Stream Warm Core Ring interaction with continental shelf and slope circulation, *Journal of Geophysical Research: Oceans*, *119*, 5968–5991, 2014.

Chen, Z., Y. O. Kwon, K. Chen, P. Fratantoni, G. Gawarkiewicz, and T. M. Joyce, Long-Term SST Variability on the Northwest Atlantic Continental Shelf and Slope, *Geophysical Research Letters*, *47*, 1–11, 2020.

Coumou, D., and S. Rahmstorf, A decade of weather extremes, *Nature Climate Change*, *2*, 491–496, 2012.

Danabasoglu, G., J. F. Lamarque, J. Bacmeister, D. Bailey, A. DuVivier, J. Edwards, L. Emmons, R. Garcia, A. Gettleman, C. Hannay, M. Holland, W. G. Large, P. Lauritzen, D. Lawrence, J. Lenaerts, K. Lindsay, W. Lipscomb, M. Mills, R. Neale, K. Oleson, B. Otto-Bliesner, A. Phillips, W. Sacks, S. Tilmes, L. van Kampenhout, M. Vertenstein, A. Bertini, J. Dennis, C. Deser, C. Fischer, B. Fox-Kemper, J. E. Kay, D. Kinnison, P. Kushner, V. Larson, M. Long, S. Mickelson, J. Moore, E. Neinhouse, L. Polvani, P. Rasch, and W. Strand, The Community Earth System Model Version 2 (CESM2), *Journal of Advances in Modeling Earth Systems*, *2*, 1–35, 2020.

Deser, C., M. A. Alexander, S.-P. Xie, and A. S. Phillips, Sea Surface Temperature Variability: Patterns and Mechanisms, *Annual Review of Marine Science*, *2*, 115–143, 2010.

Giese, B. S., H. F. Seidel, G. P. Compo, and P. D. Sardeshmukh, An ensemble of ocean reanalyses for 1815-2013 with sparse observational input, *Journal of Geophysical Research: Oceans*, *121*, 6891–6910, 2016.

Han, G., Three-dimensional seasonal-mean circulation and hydrography on the eastern Scotian Shelf, *Journal of Geophysical Research*, *108*, 2003.

Han, G., N. Chen, and Z. Ma, Is there a north-south phase shift in the surface Labrador Current transport on the interannual-to-decadal scale?, *Journal of Geophysical Research: Oceans*, *119*, 276–287, 2014.

Henson, S. A., C. Beaulieu, T. Ilyina, J. G. John, M. Long, R. Séférian, J. Tjiputra, and J. L. Sarmiento, Rapid emergence of climate change in environmental drivers of marine ecosystems, *Nature Communications*, *8*, 1–9, 2017.

Hirahara, S., M. Ishii, and Y. Fukuda, Centennial-scale sea surface temperature analysis and its uncertainty, *Journal of Climate*, *27*, 57–75, 2014.

Hobday, A., E. Oliver, A. Sen Gupta, J. Benthuysen, M. Burrows, M. Donat, N. Holbrook, P. Moore, M. Thomsen, T. Wernberg, and D. Smale, Categorizing and Naming Marine Heatwaves, *Oceanography*, *31*, 62–73, 2018.

Holbrook, N. J., H. A. Scannell, A. Sen Gupta, J. A. Benthuysen, M. Feng, E. C. Oliver, L. V. Alexander, M. T. Burrows, M. G. Donat, A. J. Hobday, P. J. Moore, S. E. Perkins-Kirkpatrick, D. A. Smale, S. C. Straub, and T. Wernberg, A global assessment of marine heatwaves and their drivers, *Nature Communications*, *10*, 1–13, 2019.

Huang, B., P. W. Thorne, V. F. Banzon, T. Boyer, G. Chepurin, J. H. Lawrimore, M. J. Menne, T. M. Smith, R. S. Vose, and H. M. Zhang, Extended reconstructed Sea surface temperature, Version 5 (ERSSTv5): Upgrades, validations, and intercomparisons, *Journal of Climate*, *30*, 8179–8205, 2017.

Hurrell, J. W., Y. Kushnir, G. Ottersen, and M. Visbeck, An overview of the north atlantic oscillation, *Geophysical Monograph Series*, *134*, 1–35, 2003.

Kay, J. E., C. Deser, A. Phillips, A. Mai, C. Hannay, G. Strand, J. M. Arblaster, S. C. Bates, G. Danabasoglu, J. Edwards, M. Holland, P. Kushner, J. F. Lamarque, D. Lawrence, K. Lindsay, A. Middleton, E. Munoz, R. Neale, K. Oleson, L. Polvani, and M. Vertenstein, The community earth system model (CESM) large ensemble project : A community resource for studying climate change in the presence of internal climate variability, *Bulletin of the American Meteorological Society*, *96*, 1333–1349, 2015.

Kent, M., E. C. Kent, and J. J. Kennedy, Historical Estimates of Surface Marine Temperatures, *Annual Review of Marine Science*, *13*, 283–311, 2021.

Laloyaux, P., E. de Boisseson, M. Balmaseda, J. R. Bidlot, S. Broennimann, R. Buizza, P. Dalhgren, D. Dee, L. Haimberger, H. Hersbach, Y. Kosaka, M. Martin, P. Poli, N. Rayner, E. Rustemeier, and D. Schepers, CERA-20C: A Coupled Reanalysis of the Twentieth Century, *Journal of Advances in Modeling Earth Systems*, *10*, 1172–1195, 2018.

Large, W. G., G. Danabasoglu, S. C. Doney, and J. C. Mcwilliams, Sensitivity to surface forcing and boundary layer mixing in a global ocean model: Annual-mean climatology, *Journal of Physical Oceanography*, *27*, 2418–2447, 1997.

Loder, J. W., and B. Petrie, The coastal ocean off Northeastern North America: A large-scale view, *This Sea*, *11*, 1998.

Loder, J. W., and Z. Wang, Trends and Variability of Sea Surface Temperature in the Northwest Atlantic from Three Historical Gridded Datasets, *Atmosphere - Ocean*, *53*, 510–528, 2015.

Loder, J. W., and Z. Wang, Seasonality of Trends and Modal Variability in Sea Surface Temperature in the Northwest Atlantic, *Atmosphere-Ocean*, pp. 1–61, 2019.

Lotze, H. K., M. Stefanie, J. Coyne, M. Betts, M. Burchell, K. Fennel, M. A. Dusseault, E. Galbraith, L. Garcia Suarez, L. de Gelleke, N. Golombek, B. Kelly, S. D. Kuehn, E. Oliver, M. MacKinnon, W. Muraoka, I. T. Predham, K. Rutherford, O. Sherwood, E. C. Sibert, M. Kienast, S. D. Fuller, and N. Shackell, Long-term ocean and resource dynamics in a hotspot of climate change, *FACETS*, In Review.

Marshall, J., Y. Kushnir, D. Battisti, P. Chang, A. Czaja, R. Dickson, J. Hurrell, M. McCartney, R. Saravanan, and M. Visbeck, North Atlantic climate variability: Phenomena, impacts and mechanisms, *International Journal of Climatology*, *21*, 1863–1898, 2001.

Mills, K. E., A. J. Pershing, C. J. Brown, Y. Chen, F.-S. Chiang, D. S. Holland, S. Lehuta, J. A. Nye, J. C. Sun, A. C. Thomas, and R. A. Wahle, Fisheries Management in a Changing Climate, *Oceanography*, *26*, 191–195, 2013.

Moisan, J. R., and P. P. Niiler, The seasonal heat budget of the North Pacific: Net heat flux and heat storage rates (1950-1990), *Journal of Physical Oceanography*, *28*, 401–421, 1998.

O'Carroll, A. G., J. R. Eyre, and R. W. Saunders, Three-way error analysis between AATSR, AMSR,E, and in situ sea surface temperature observations, *Journal of Atmospheric and Oceanic Technology*, *25*, 1197–1207, 2008.

Oliver, E. C., M. G. Donat, M. T. Burrows, P. J. Moore, D. A. Smale, L. V. Alexander, J. A. Benthuysen, M. Feng, A. Sen Gupta, A. J. Hobday, N. J. Holbrook, S. E. Perkins-Kirkpatrick, H. A. Scannell, S. C. Straub, and T. Wernberg, Longer and more frequent marine heatwaves over the past century, *Nature Communications*, *9*, 1–12, 2018.

Oliver, E. C. J., J. A. Benthuysen, S. Darmaraki, M. G. Donat, J. Hobday, N. J. Holbrook, W. Robert, and A. S. Gupta, Marine Heatwaves, *Annual Review of Marine Science*, pp. 1–30, 2021.

Overland, J. E., and R. W. Preisendorfer, Significance test for principal components applied to a cyclone climatology., *Monthly Weather Review*, *110*, 1–4, 1982.

Petrie, B., Does the North Atlantic Oscillation affect hydrographic properties on the Canadian Atlantic Continental Shelf?, *Atmosphere - Ocean*, *45*, 141–151, 2007.

Petrie, B., and K. Drinkwater, Temperature and Salinity Variability on the Scotian Shelf and in the Gulf of Maine 1945-1990, *Journal of Geophysical Research*, *98*, 20079–20089, 1993.

Rayner, N. A., D. E. Parker, E. B. Horton, C. K. Folland, L. V. Alexander, D. P. Rowell, E. C. Kent, and A. Kaplan, Global analyses of sea surface temperature, sea ice, and night marine air temperature since the late nineteenth century, *Journal of Geophysical Research D: Atmospheres*, *108*, 2003.

Richaud, B., Y. O. Kwon, T. M. Joyce, P. S. Fratantoni, and S. J. Lentz, Surface and bottom temperature and salinity climatology along the continental shelf off the Canadian and U.S. East Coasts, *Continental Shelf Research*, *124*, 165–181, 2016.

Rodgers, K. B., S.-S. Lee, N. Rosenbloom, A. Timmermann, G. Danabasoglu, C. Deser, J. Edwards, J.-E. Kim, I. Simpson, K. Stein, M. F. Stuecker, R. Yamaguchi, T. Bodai, E.-S. Chung, L. Huang, W. M. Kim, J.-F. Lamarque, D. L. Lombardozzi, W. R. Wieder, and S. G. Yeager, Ubiquity of human-induced changes in climate variability, *EarthArxiv*, 2021.

Roemmich, D., J. Gilson, J. Willis, P. Sutton, and K. Ridgway, Closing the time-varying mass and heat budgets for large ocean areas: The Tasman Box, *Journal of Climate*, *18*, 2330–2343, 2005.

Sachs, J. P., Cooling of Northwest Atlantic slope waters during the Holocene, *Geophysical Research Letters*, *34*, 1–4, 2007.

Schlegel, R. W., E. C. Oliver, and K. Chen, Drivers of Marine Heatwaves in the Northwest Atlantic: The Role of AirSea Interaction During Onset and Decline, *Frontiers in Marine Science*, *8*, 1–18, 2021.

Shearman, R. K., and S. J. Lentz, Long-term sea surface temperature variability along the U.S. East Coast, *Journal of Physical Oceanography*, *40*, 1004–1017, 2010.

Stevenson, J. W., and P. P. Niiler, Upper Ocean Heat Budget During the Hawaii-to-Tahiti Shuttle Experiment, *Journal of Physical Oceanography*, *13*, 1894–1907, 1983.

Trenberth, K. E., and D. J. Shea, Atlantic hurricanes and natural variability in 2005, *Geophysical Research Letters*, *33*, 1–4, 2006.

Visbeck, M., E. P. Chassignet, and B. Dickson, 6 . The Ocean ' s Response to North Atlantic Oscillation Variability, *Geophysical Monograph Series*, *134*, 113–145, 2003.

Wills, R. C., K. C. Armour, D. S. Battisti, and D. L. Hartmann, Ocean-atmosphere dynamical coupling fundamental to the atlantic multidecadal oscillation, *Journal of Climate*, *32*, 251–272, 2019.